The Meteoritical Society

*Meteoritics & Planetary Science* 44, Nr 10, 1519–1540 (2009)
Abstract available online at http://meteoritics.org

# Along-track compositional and textural variation in extensively melted grains returned from comet 81P/Wild 2 by the Stardust mission: Implications for capture-melting process

Michael A. VELBEL[1*] and Ralph P. HARVEY[2]

[1]Department of Geological Sciences, 206 Natural Science Building, Michigan State University, East Lansing, Michigan 48824–1115, USA
[2]Department of Geological Sciences, Case Western Reserve University, Cleveland, Ohio 44106, USA
[*]Corresponding author. E-mail: velbel@msu.edu

*(Received 23 July 2008; revision accepted 02 May 2009)*

**Abstract**–Five amorphous (extensively melted) grains from Stardust aerogel capture Track 35 were examined by transmission electron microscopy (TEM); two from the bulb, two from near the bulb-stylus transition, and one from near the terminal particle. Melted grains consist largely of a texturally and compositionally heterogeneous emulsion of immiscible metal/sulfide beads nanometers to tens of nanometers in diameter in a silica-rich vesicular glass. Most metal/sulfide beads are spherical, but textures of non-spherical beads indicate that some solidified as large drops during stretching and breaking while in translational and rotational motion, and others solidified from lenses of immiscible liquid at the silicate-melt/vesicle (vapor) interface.

Melted grains appear to become richer in Fe relative to Mg, and depleted in S relative to Fe and Ni with increasing penetration distance along the aerogel capture track. Fe/S ratios are near unity in grains from the bulb of Track 35, consistent with the dominance of Fe-monosulfide minerals inferred by previous research on Stardust materials. Near-stoichiometric Fe/S in melted grains from the bulb suggests that Fe-sulfides in the bulb were dispersed and melted during formation of the bulb but did not lose S. Along-track increases in Fe/S in melted grains from the bulb through the bulb-stylus transition and continuing into the stylus indicate that S initially present as iron monosulfide may have been progressively partially volatilized and lost from the melted grains with greater penetration of the grains deeper into the aerogel during capture-melting of comet dust. Extensively melted grains from the bulbs of aerogel capture tracks may preserve better primary compositional information with less capture-related modification than grains from farther along the same capture tracks.

## INTRODUCTION

NASA's Stardust mission sampled and returned to Earth micrometer-scale fragments of dust from comet 81P/Wild 2. Comet dust particles were captured in silica aerogel (Hörz et al. 2001, 2006; Bernhard et al. 2001; Brownlee et al. 2006; Zolensky et al. 2006, 2008a, 2008b; Stephan 2008; Flynn 2008; Leroux et al. 2008a). Many of the grains captured by the Stardust spacecraft during its encounter with comet 81P/Wild 2 consist of crystalline phases (predominantly the silicate minerals olivine and/or pyroxene, with less abundant but ubiquitous Fe-Ni sulfides; Zolensky et al. 2006, 2008b; Hörz et al. 2006; Nakamura et al. 2008a, 2008b; Tomeoka et al. 2008; Leroux et al. 2008b) and amorphous silica-rich material (Zolensky et al. 2006; Leroux et al. 2008a, 2009; Nakamura et al. 2008a; Tomeoka et al. 2008; Roskosz et al. 2008). However, the orbital trajectory that allowed the spacecraft to encounter comet 81P/Wild 2, image its nucleus during flyby, intersect the comet's coma for dust sampling, and return to Earth, required a spacecraft-comet relative velocity of ~6.1 km $s^{-1}$ (Brownlee et al. 2006). Consequently, the aerogel capture process involved conversion of kinetic energy to other forms of energy, including heat that resulted in extensive melting of many fragments (Anderson and Ahrens 1994; Dominguez et al. 2004; Brownlee et al. 2006; Zolensky et al. 2006; Ishii et al. 2008a; Leroux et al. 2008a, 2009; Trigo-Rodríguez et al. 2008; Nakamura et al. 2008a; Tomeoka et al. 2008; Roskosz et al. 2008). Heating effects during particle capture varied widely, from preservation of crystalline phases in multiphase aggregates to complete melting (Zolensky et al. 2006; Brownlee et al. 2006; Leroux et al.

2008a; 2009); in some occurrences, the entire range can be observed in a single object (Tomeoka et al. 2008).

A variety of features of extensively to completely melted Stardust grains examined to date are described by Zolensky et al. (2006), Leroux et al. (2008a, 2009), Nakamura et al. (2008a), and Tomeoka et al. (2008). Transmission electron microscope (TEM) imagery from numerous extensively melted, glassy grains reveals fractured grains in which voids and breakage exhibit a preferred orientation parallel to the long dimension of the particle. The chattering (which is more distinct in higher-magnification images) is an artifact of flexural stresses fracturing brittle material during ultramicrotomy (Bradley 1988; Zolensky et al. 2008a; Leroux et al. 2008a; Tomeoka et al. 2008; Rietmeijer et al. 2008), as it does not occur on the grain in the potted butt from which the ultramicrotome slices were taken or in amorphous grains examined by synchrotron microtomography (Nakamura et al. 2008a). Extensively melted grains consist of vesicular glassy material with dark inclusions as described by Zolensky et al. (2006, Figs. 1A and B), Leroux et al. (2008a, 2009) and Tomeoka et al. (2008). Energy dispersive spectroscopy (EDS) analyses of low-magnification fields-of-view suggest broadly chondritic ratios of elements indigenous to the cometary particles (Leroux et al. 2008a, 2009; Tomeoka et al. 2008; Rietmeijer et al. 2008); for example, Leroux et al. (2008a, 2009) found bulk major element compositions of glassy Stardust grains (including sulfur) to be a near-perfect match with CI composition. Grains affected by partial or complete melting are compositionally heterogeneous, reflecting the small size and heterogeneous distribution of minerals in the pre-capture comet-dust particle, and extensive mixing of partly to completely melted comet material with molten aerogel (Zolensky et al. 2006; Leroux et al. 2008a).

Compositional heterogeneity in the melt-modified material is consistent with melting of a variety of silicate- and sulfide-metal-rich volumes of incident Stardust particles of chondritic composition (Leroux et al. 2008a, 2009; Stephan 2008; Stephan et al. 2008). Leroux et al. (2008a) inferred multiple varieties of olivine and pyroxenes to be the precursors of the heterogeneous silicate glass, and sulfide minerals likely melted and re-solidified to form the metal-sulfide objects dispersed throughout the silicate glass. Leroux et al. (2009) suggested formation of metal-sulfide beads by reduction of initially silicate-hosted Fe to metal during thermal modification, followed by sulfidation of metal during cooling. In all models proposed to date, the inferred precursor minerals resemble the silicates, sulfides, and metals observed in unmelted portions of other Stardust grains (Brownlee et al. 2006; Zolensky et al. 2006, 2008b; Ishii et al. 2008a; Nakamura et al. 2008a, 2008b; Tomeoka et al. 2008; Leroux et al. 2008b).

Vesicularity in the glassy material is attributed to evolution of gases from heated aerogel (Leroux et al. 2008a), partial volatilization of sulfur from sulfides (Tomeoka et al. 2008), and/or evolution of CO produced by oxidation of aerogel-contaminant and/or indigenous carbon during reduction of Fe at high temperature (Leroux et al. 2009). Glass that is Mg-rich and inferred to include a melted olivine or pyroxene fraction is not vesicular (Leroux et al. 2008a), suggesting that the pre-capture silicate precursors of non-vesicular glass volumes were anhydrous and that neither the anhydrous pre-capture silicates nor the admixed molten aerogel that dilutes the olivine/pyroxene signature evolved volatiles upon heating during capture. If the abundant vesicularity noted in melted Stardust grains was not caused by evolution from aerogel, then volatile species must be abundant within one or more projectile phases.

The purposes of this paper are to describe and interpret two sets of melting-related properties in a suite of five aerogel-capture-modified Stardust grains from several locations along a single capture track:

1. Relationships between solidified, formerly molten metal-sulfide droplets and their surroundings are investigated through morphological classification of the observed variety of sulfide-metal textures and associations. Much of the morphological variation in the entire population of melted sulfide-metal grains reported from previous work is present in this ensemble of allocations from this single track. This paper briefly describes sulfide-metal occurrences that were reported as widely occurring by Leroux et al. (2008a), but emphasizes textures and associations that were not commonly enough observed in the overall ensemble of melted grains examined by previous workers to warrant detailed discussion. Several new inferences can be drawn from these observations that add detail to the variety of phenomena that have been documented by previous work.
2. Bulk compositions for different analyzed areas within individual grains are examined for five aerogel-capture-modified Stardust grains from several locations along a single capture track.

Compositional analyses of large imaged areas characterize compositional heterogeneity in products of capture melting at the ~10 micron scale. Comparing ranges of compositions between different discrete but adjacent grains at similar positions along the aerogel-capture track characterizes heterogeneity of pre-disrupted, pre-capture particles and/or the capture-melting process at scales larger than 10–20 microns. Comparing compositional ranges and means for suites of melted fragments from multiple locations along individual capture tracks will allow (a) systematic along-track variations to be distinguished from other forms of compositional heterogeneity, and (b) assessment of along-track size- and density-sorting and volatile-element redistribution as influences on the chemical and

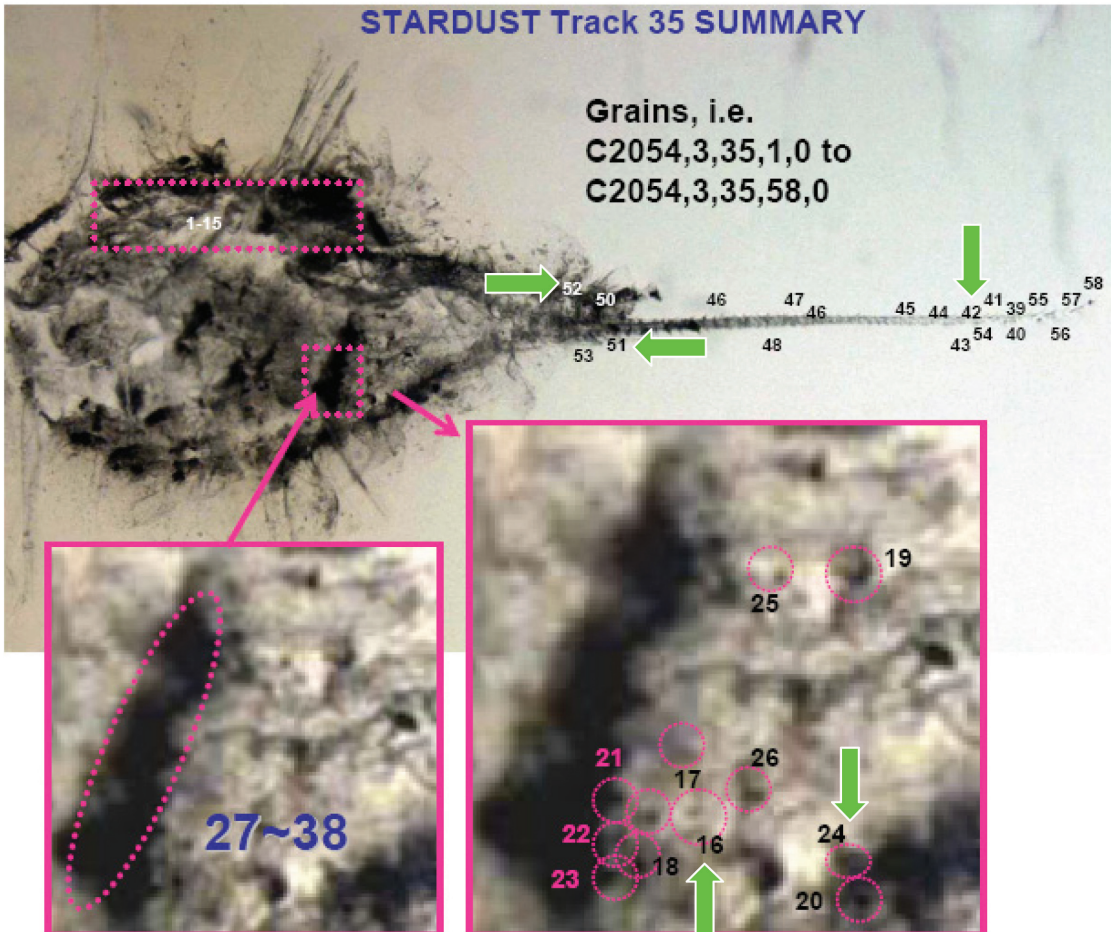


Fig. 1. Track 35 after compression and before extraction of individual grains. In this cross section view, the comet-dust particle entered the field of view at the left moving to the right with an initial relative velocity of 6.1 km $s^{-1}$. After forming the entry aperture at the left edge of the image, energetic disruption of the particle into small fragments formed a large bulb. With continued penetration into the aerogel (continued movement of comet-dust debris from left to right), some fragments penetrated farther (to the right), forming the stylus. Grain 58 was the terminal particle. The length of Track 35 (the distance from the entry aperture to grain 58) is 11.7 mm. The arrows indicate locations of the five allocations examined for this study. Figure courtesy K. Nakamura-Messenger.

mineralogical properties of individual grains and whole aerogel tracks.

## MATERIALS AND METHODS

### Materials Examined

#### *Aerogel Capture Track Nomenclature*

Track 35 (Fig. 1) is an 11.7 mm long bulbous (type B) track that was one of the first to be recognized and extracted during preliminary examination; it is the track illustrated on the cover of the 15 December 2006 Stardust issue of *Science*. The tracks along which crystalline and amorphous comet-dust debris are distributed vary in shape, with varying degrees of development of two features; the bulb and the stylus. Track 35 has both (Fig. 1). The bulb is a large debris-lined cavity immediately inside the entry aperture, formed by rapid disruption of the projectile (especially a projectile that is a porous aggregate of smaller grains) upon initial deceleration and radial dispersal of the debris (Anderson and Ahrens, 1994; Burchell et al. 2006; Trigo-Rodríguez et al. 2008). The stylus is a long, narrow feature that extends further into the aerogel. Type B tracks are shaped like champagne flute wine glasses without the base (bowl and stem only; Hörz et al. 2006; Burchell et al. 2008).

The bulb and stylus are produced by the interaction of different varieties of debris from the fragmentation of the incident particle. Hypervelocity impact produces a spray of fragments radiating from the point of impact, with a velocity distribution such that fragments with trajectories away from the impact point at the lowest spray angles (moving near-parallel to the trajectory of the projectile) have the highest velocities (nearly equal to the velocity of the projectile), and fragments moving at higher spray angles have significantly lower velocities (Akahoshi et al. 2003). Strong projectiles that do not produce clouds of fragments penetrate deeply into the capture medium and create carrot shaped tracks (all stylus, Type A) whereas weak projectiles that fragment upon impact

generate fragment clouds with a radial distribution of fragments that do not penetrate as deeply (producing a track that is all bulb, Type C; Hörz et al. 2006; Burchell et al. 2008). Weak projectiles with included strong portions form a Type B track, with the bulb produced from the high-angle dispersion of fine debris away from the impact point, and the stylus from the stronger components penetrating farther into the capture medium along a trajectory more parallel to the incidence angle of the impacting particle (Hörz et al. 2006; Burchell et al. 2008). Most large Stardust tracks (including the one examined here) exhibit both bulb and stylus. A stylus ends at a visible "terminal" particle. Bifurcating tracks and smaller stylus-like projections radiating from bulbs (called "subtracks" by some workers) also end in particles referred to by some researchers as "terminal particles." The morphology of Track 35 suggests the incident comet dust particle was a fragile aggregate of easily fragmented material with some inclusions of mechanically stronger material.

### *Allocation Nomenclature*

Following Tsou (personal communication, 2006; see also description of nomenclature conventions by Flynn 2008), the term "particles" is used here when referring to the (inferred) pre-capture projectiles; the terms "grains" and "fragments" are used for the captured solids extracted from the aerogel capture medium. Each incident comet-dust particle was disrupted during capture and disaggregated into numerous fragments or grains distributed along the track through the aerogel capture medium, each of which is extracted and examined individually.

The object at the end of a stylus in the capture track is widely termed a "terminal particle." The terminal particle is extracted from the end of a stylus in a capture track; the inferred pre-capture object (referred to by Tsou as a "particle"; Flynn 2008) is termed an "incident (comet-dust) particle" in this paper, to more clearly distinguish the inferred pre-capture aggregate entity from the discrete object extracted from the end of a stylus of an aerogel capture track.

Grains (or fragments) consisting entirely of multiple crystalline phases are rocks (Burnett 2006); they are referred to here as microrocks in recognition of their size and to distinguish them from captured grains consisting of single crystals or amorphous material. Grains consisting predominantly or exclusively of amorphous (melted and quenched) material (and termed amorphous during Stardust Preliminary Examination (PE), e.g., Zolensky et al. 2006) are referred to as melted grains, following Leroux et al. (2008a). The terminology of "grains" within grains remains unresolved. Individual objects within fragments or grains and consisting of identifiable minerals are called "crystals" if they exhibited diffraction effects in TEM, selected area electron diffraction (SAED) or synchrotron X-ray diffraction (SXRD). The term "bead" is used (e.g., Ishii et al. 2008b) for small rounded metal-sulfide objects dispersed throughout the silica-rich glass that constitutes the dominant portion of individual glassy, predominantly amorphous melted grains.

### *Allocation Numbering System*

Aspects of the Stardust allocation numbering system relevant to this paper are summarized here, excerpted from the Stardust Cometary Sample Catalog (Bastien et al. 2006). The first portion is the identification number of the parent aerogel cell, for example C2054. The second part of the allocation name is the number of the separated aerogel piece that contains the captured particle. The parent piece is number 0, with subsequent subdivisions numbered in sequence beginning with 1. The third part of an allocation number is the number given to the aerogel track extracted from the separated aerogel piece. Tracks are numbered sequentially in order of their removal from aerogel cells and/or first sampling. The fourth number corresponds to a specific grain in the aerogel piece. The last number is the sample mount (in this study, TEM grid) number. For example the allocation C2054,0,35,16,8 is the TEM grid 8, made from grain 16, from track 35, which was located in the main aerogel piece (0) removed from aerogel cell C2054. Each TEM grid has four ultramicrotome slices, each numbered sequentially in order of preparation from a given grain.

### *Allocations from Track 35 Examined in This Study*

This paper describes the micron-scale bulk-composition of melted grains, and nanometer-scale petrography of sulfides and metals, in five large and almost completely melted Stardust fragments from various places along a single aerogel-capture track. Grains dominated by (preserved, indigenous cometary) crystalline matter and (extensively melted) amorphous matter both occur all along Track 35 (Zolensky et al. 2006). All allocations from Track 35 examined by Leroux et al. (2008a) and Tomeoka et al. (2008) are glassy. More than 75% of the grains from Track 35 examined by Nakamura et al. (2008a) are glassy, although several are microrocks with mineral assemblages, textures, and oxygen isotope systematics very similar to carbonaceous chondrites (Nakamura et al. 2008b). Fragments from other allocations in this track exhibit extreme values of several parameters among suites of Stardust allocations examined by a variety of methods. A fragment from the bulb of Track 35 (grain 20) gave infrared spectral (Si-O stretching) indications of a higher degree of mixing with aerogel than any other grain described by Keller et al. (2006) from any track. Grain 16 (also from the bulb of Track 35) has the highest Mg/Fe ratio, and grain 45 (from the stylus) has the lowest, among all allocations examined using TOF-SIMS by Stephan et al. (2008). Extensively melted grains along Track 35 appear to encompass the most extreme range of compositional heterogeneity found to date in Stardust allocations; Track 35 is thus well suited for study of compositional attributes associated with melting of comet dust during aerogel capture.

Table 1. Allocations analyzed in this study.

| Curatorial designation | Short name | Aerogel depth (mm) | Slice thickness (nm) | Other studies of different allocations from same grains: TEM | TOF-SIMS |
|---|---|---|---|---|---|
| C2054,0,35,16,8 | Grain 16 | 3.51 | 100 | Leroux et al. (2008a), 16,1 16,2, 16,8; Tomeoka et al (2008), 16,6 | Stephan et al. (2008) 16,9 |
| C2054,0,35,24,8 | Grain 24 | 3.67 | 140 | Leroux et al. (2008a), 24,1 24,7 | Stephan et al. (2008) 24,5 |
| C2054,0,35,42,3 | Grain 42 | 10.38 | 70 | | |
| C2054,0,35,51,4 | Grain 51 | 6.08 | 70 | Leroux et al. (2008a), 51,3; Leroux et al. (2009), 51,3 | |
| C2054,0,35,52,6 | Grain 52 | 6.55 | 70 | Leroux et al. (2008) 52,3 | |
| | | | | Other studies of other allocations from the same track: | |
| | | | | Nakamura et al. (2008), SEM & SXRD | |
| | | | | Tomeoka et al. (2008), TEM | |
| | | | | Stephan et al. (2008), TOF-SIMS | |

Five amorphous grains from Track 35 were examined; two from the bulb, two from near the bulb-stylus transition, and one from near the terminal particle (Fig. 1). Grains 16 and 24 are from the bulb portion of Track 35, and were within approximately 1 mm of each other prior to extraction from compressed aerogel. Grains 51 and 52 are from within approximately 1 mm of each other near the bulb-stylus transition, with 52 within the bulb and 51 in the stylus. Grain 42 was extracted from the stylus portion of the track, within a few mm of the terminal particle.

In this paper, grains are discussed in relation to their position along Track 35 (Fig. 1). Melted grains extracted from the bulb (grains 16 and 24) are distinguished from those extracted from the bulb-stylus transition (grains 51 and 52), and from the stylus (grain 42). "Along-track" refers to different distances from the entry aperture. "Downtrack" refers specifically to greater penetration distance; grains from the bulb-stylus transition (51 and 52) and from the stylus (42) are downtrack of the bulb and the grains (16 and 24) extracted from the bulb.

**Methods: Electron Microscopy**

All allocations were prepared at NASA JSC as part of the Stardust Preliminary Examination (PE) effort. Procedures and methods are described in detail by Matrajt and Brownlee (2006) and Zolensky et al. (2008a). Allocations examined in this study include the remnant of one fragment as exposed on the surface of the potted butt (C2054,0,35,16,0, imaged and described by Zolensky et al. 2008a, Fig. 9, and examined here by scanning electron microscopy [SEM]), and five TEM grids (Table 1) each containing four serial ultramicrotome slices on the holey carbon support of a 3 mm diameter Cu TEM grid (examined by TEM and scanning transmission electron microscopy [STEM]). The twenty ultramicrotome slices (four each from five grains) were examined in the JEOL 2200FS field-emission gun (FEG)-TEM equipped with an Oxford energy dispersive spectroscopy (EDS) system, at MSU's Center for Advanced Microscopy (CAM), at 200kV accelerating voltage. The ultramicrotome slices ranged in thickness from 70 nm to 140 nm thick; specific values for each slice (Table 1; from K. Nakamura-Messenger, written communication) were used in EDS data reduction. Images were acquired for large areas and individual minerals by bright-field TEM and STEM imaging; compositional data were acquired using EDS in TEM and STEM modes; and structural data by SAED in TEM mode. Basic sample characteristics and most of our mineralogical data are mostly similar to those reported from Track 35 allocations by previous workers (Tables 1 and 2), so only textural and bulk-compositional data are reported here.

Several elements were excluded from quantification of EDS data: Si and O were excluded because these elements include contamination of the grain by mixing with the same elements from the aerogel capture medium; Cu and C were excluded because these elements constitute the TEM grid and the holey carbon support, respectively; and Cl was excluded because its abundance is affected by contamination from the epoxy used to embed the grain prior to ultramicrotomy. Although Ca, Fe, Ni, Cu, and Zn are known to occur as contaminants in track-free flight aerogel (Flynn et al. 2006, supplementary online material), they occur at parts per million abundances that are unlikely to influence our weight-percent-level analyses. Elements detected in this study by TEM-EDS which likely represent essentially uncontaminated comet material are Mg, Ca, Fe, Ni, Cr, and S.

## RESULTS

All extracted grains from the five Track 35 allocations examined by TEM consist of vesicular glassy material with dark inclusions, identical to common Stardust material as described by Zolensky et al. (2006, Figs. 1A and B), Leroux et al. (2008a, 2009), and Tomeoka et al. (2008). (To conserve space, this paper does not include images or

analytical data illustrating additional examples of common features similar to those imaged in other papers.)

## Morphology of Beads

Rounded objects darker (electron-opaque at the applied accelerating voltage) in bright-field TEM than the vesicular glass are ubiquitous in all grains from Track 35 examined here, as in many similar grains (Leroux et al. 2008a; Tomeoka et al. 2008). Rounded objects (beads) are very common and widely distributed in the five grains allocated for this study, as in many other grains (Zolensky et al. 2006, 2008b; Ishii et al. 2008a; Leroux et al. 2008a; Rietmeijer et al. 2008; Tomeoka et al. 2008). The beads range in diameter from tens of nanometers or smaller to more than 100 nm (Leroux et al. 2008a). Shapes are predominantly spherical (circular cross sections in TEM imagery) with elongate or oblate rounded forms locally abundant, and a few occurrences of angular grains. Rounded objects are termed "beads" (e.g., Ishii et al. 2008b), without genetic connotation.

Leroux et al. (2008a) reported two categories of internal arrangements of minerals in Fe-Ni-S beads; (1) smaller, homogenous fine-scale intergrowths of kamacite and pyrrhotite, and (2) larger objects with a "core-mantle texture". Where both types are being discussed as a single population, the term "beads" is used here. Where evidence indicates multiple phases, terms such as "two-phase beads" will be used. The interior phase can be described as the core with minimal risk of confusion, but because material identical to the mantles of Leroux et al. (2008a) has been observed without a core to mantle, such material could also be described as a shell (either surrounding the core of a bead, or separated and isolated from any core, most likely during sample preparation).

Sulfides and metal both occur predominantly as beads in this study as in others (Table 2). A very small number of angular mineral grains that may not been completely melted during aerogel capture occur in grain 16; lacking definitive textural evidence of their relation to the rounded, melted beads, the angular mineral grains from melted grain 16 are not discussed further here. The rounded beads are in all discernible ways identical to those reported previously. Because of their strong similarity to those reported by numerous previous workers, new observations of spherical beads from Track 35 examined for this study are not discussed further. Most rounded inclusions (beads) in the allocations examined here contain both metal and sulfide and are identical to many described by Zolensky et al. (2006, 2008b), Ishii et al. (2008a), Leroux et al. (2008a, 2009), Rietmeijer et al. (2008), and Tomeoka et al. (2008). To facilitate comparison with previous work and to illustrate the range of inclusion compositions present in a single melted grain (relative to other inclusions in other melted grains), EDS analyses for a number of spot analyses of metal and sulfide objects in grain 16 (including angular nanometer-scale grains, common metal-sulfide beads, and uncommon varieties of beads) are shown in Fig. 2.

Individual spherically symmetric beads are by far the most common bead shape in the grains from Track 35 examined here, as in others (Zolensky et al. 2006, 2008b; Ishii et al. 2008b; Leroux et al. 2008a, 2009; Rietmeijer et al. 2008; Tomeoka et al. 2008). However, a number of non-spherical morphologies of Fe-Ni-S inclusions also occur in melted grains (Leroux et al. 2008a). Deviations from circular-spherical symmetry include oblate forms symmetric about their short axes (elongate or elliptical in cross section; Fig. 3; see also Leroux et al. 2008a, Fig. 11d). Elongate forms occur along the interfaces between silica-rich glass and vesicles (Fig. 3). Along straight, gently concave, and convex glass-vesicle interfaces metal-sulfide beads are lenticular, with long axes aligned parallel to the glass-vesicle interface (Fig. 3). Lenses extend more deeply into the silica-rich glass than into the vesicle (Fig. 3); this is especially well-developed at strongly curved concave glass-vesicle interfaces (Figs. 3d, 3e).

Asymmetric varieties include those with spherical cores and thicker non-spherical shells (Fig. 3d); non-spherical or non-oblate cores with thin conforming shells Fig. 4a; see also Leroux et al. 2008a, Fig. 10) or thicker non-conforming shells (Fig. 4b); irregular cores with irregular envelopes (Leroux et al. 2008a, Fig. 11a; not discussed further here), and compound beads in which two distinct cores are enveloped by continuous shell material (Fig. 5; Leroux et al. 2008a, Figs. 11b and 11c illustrate, describe and discuss other examples).

## Compositions of Melted Glassy Grains

Averages of multiple EDS analyses of low-magnification fields-of-view for each allocation are shown in Table 3, as percentages of elements indigenous to the cometary particles (Mg, Fe, Ni, S, Ca, Cr), excluding elements likely modified in abundance by mixing of molten cometary matter with molten aerogel (Leroux et al. 2008a). The bulk composition (and comet-dust/aerogel mixing relations) of the material described here from grain 16 were among those reported by Leroux et al. (2008a, their Table 3). Data for the other four allocations are reported here for the first time. For comparison Table 3 also shows an average composition based on all five Stardust allocations examined for this study, and abundances similarly calculated for CI (Leroux et al. 2008a).

Relationships and trends among elements of interest are shown in scatter plots of Fe versus S (Fig. 6), Fe/Mg versus S/Mg (Fig. 7), and Ni versus S (Fig. 8), and plots of Fe/Mg (Fig. 9), Fe/S (Fig. 10) and (Fe + Ni)/S (Fig. 11) as a function of grain penetration depth into aerogel. Chemical composition varies modestly within individual grains, and considerably between adjacent grains. Ranges for major elements (e.g., Mg, Fe, Ca) are generally small among different analyzed areas within the same grain (Figs. 6–11).

Table 2. Sulfide and metal minerals previously identified in Track 35 and other Stardust tracks.

| Mineral | Formula | In terminal grain | In microrock | Angular grain | Core-mantle droplet core | Core-mantle droplet shell | Fine-scale polycrystalline intergrowth | Melted grain, unspecified | Other | Grain# | Bulb or stylus? | Method(s) | Reference(s) |
|---|---|---|---|---|---|---|---|---|---|---|---|---|---|
| *In other extensively melted grains* | | | | | | | | | | | | | |
| Troilite | FeS | | | | | | | | | | | | |
| Pyrrhotite | $Fe_{(1-x)}S$ | X | X | | | | | | Assoc. w/enstatite, f.g. mat'l; and pentlandite | | TEM EDS | Brownlee et al. 2006 | |
| Pyrrhotite | $Fe_{(1-x)}S$ | | | | | | | X | Mixed w/kamacite | | | TEM EDS, SAED | Rietmeijer et al. 2005 |
| Pyrrhotite | $Fe_{(1-x)}S$ | | | | | | | X | Unspecified | | | TEM EDS, SAED | Rietmeijer et al. 2006 |
| Pyrrhotite | $Fe_{(1-x)}S$ | | | | | | | X | | | | TEM SAED | Zolensky et al. 2008b |
| Pyrrhotite | $Fe_{(1-x)}S$ | | | | | | X | | Mixed w/kamacite | | | TEM SAED | Leroux et al. 2008a |
| Fe-monosulfide (unspecified) | FeS | | | | | X | | | | | | TEM EDS | Ishii et al. 2008a |
| Fe-monosulfide (unspecified) | FeS | X | | | | | | | Mixed w/metal | | | TEM EDS, SAED | Zolensky et al. 2006 |
| Fe-monosulfide (unspecified) | FeS | | | | | | | | Mixed w/metal | | | TEM EDS, SAED | Tomeoka et al. 2008 |
| Fe-monosulfide (unspecified) | FeS | | | | | X | | | Multiple occurrences | | | TEM EDS, EFTEM | Leroux et al. 2008a |
| Pentlandite | $(Fe,Ni)_9S_8$ | X | X | | | | | | Assoc. w/enstatite, pyrrhotite | | | TEM EDS | Brownlee et al. 2006 |
| Pentlandite | $(Fe,Ni)_9S_8$ | | | | | | | | | | | TEM EDS | Zolensky et al. 2006 |
| Pentlandite | $(Fe,Ni)_9S_8$ | | | | | | | | | | | TEM EDS | Zolensky et al. 2006 |
| Fe-Ni sulfide (unspecified) | | | | | | | | | | | | TEM EDS, SAED | Zolensky et al. 2006 |
| Kamacite | low-Ni Fe,Ni | | | | | | | X | Mixed w/pyrrhotite | | | TEM EDS, SAED | Rietmeijer et al. 2005 |
| Kamacite | low-Ni Fe,Ni | | | | | | | X | | | | TEM EDS, SAED | Tomeoka et al. 2008 |
| Kamacite | low-Ni Fe,Ni | | | | | | X | | Mixed w/pyrrhotite | | | TEM SAED | Leroux et al. 2008a |
| Taenite | high-Ni Fe,Ni | | | | | | | | | | | | |
| Fe-Ni metal (unspecified) | Fe,Ni | X | X | | | | | | Mixed w/sulfide | | | TEM EDS, SAED | Zolensky et al. 2006 |
| Fe-Ni metal (unspecified) | Fe,Ni | | | | X | | | | | | | TEM EDS | Ishii et al. 2008a |
| Fe-Ni metal (unspecified) | Fe,Ni | | | | X | | | | Multiple occurrences | | | TEM EDS, EFTEM | Leroux et al. 2008a |
| *In craters on Al foil* | | | | | | | | | | | | | |
| Fe-monosulfide (unspecified) | FeS | | | | | | | | Crater residue | | | SEM, EDS | Hörz et al. 2006 |
| *In Track 35* | | | | | | | | | | | | | |
| Troilite | FeS | | ? | | | | | | | 5 | Bulb | SXRD and microtomography | Nakamura et al. 2008a |
| Pyrrhotite | $Fe_{(1-x)}S$ | | ? | | | | | | | 5 | Bulb | SXRD and microtomography | Nakamura et al. 2008a |
| Pyrrhotite | $Fe_{(1-x)}S$ | | | X | | | | | Assoc. w/kamacite, taenite | 51 | Transi-tion | TEM SAED | Leroux et al. 2008a |
| Pyrrhotite | $Fe_{(1-x)}S$ | X1 | X | | | | | | Assoc. w/kamacite, taenite, low-Ca px | 62 | TP1Sub trackI | SXRD and microtomography | Nakamura et al. 2008a |

Table 2. *Continued.* Sulfide and metal minerals previously identified in Track 35 and other Stardust tracks.

| Mineral | Formula | In terminal grain | In microrock | Angular grain | Core-mantle droplet core | Core-mantle droplet shell | Fine-scale polycrystalline intergrowth | Melted grain, unspecified | Other | Grain# | Bulb or stylus? | Method(s) | Reference(s) |
|---|---|---|---|---|---|---|---|---|---|---|---|---|---|
| Fe-monosulfide (unspecified) | FeS | | | | | X | | | | 16 | Bulb | TEM EDS, EFTEM | Leroux et al. 2008a |
| Kamacite | low-Ni Fe,Ni | | | X | | | | | Assoc. w/pyrrhotite, taenite | 51 | Transi-tion | TEM SAED | Leroux et al. 2008a |
| Kamacite | low-Ni Fe,Ni | | X | | | | | | | 49 | Stylus | SXRD and microtomography | Nakamura et al. 2008a |
| Kamacite | low-Ni Fe,Ni | X1 | X | | | | | | Assoc. w/Fo-rich ol, Ca-poor px, spinel and glass | 6 | TP1Sub trackC | SXRD and microtomography | Nakamura et al. 2008a,b |
| Kamacite | low-Ni Fe,Ni | X1 | X | | | | | | Assoc. w/taenite, pyrrhotite, low-Ca px | 62 | TP1Sub trackI | SXRD and microtomography | Nakamura et al. 2008a |
| Taenite | high-Ni Fe,Ni | | | | | | | X | | 16 | Bulb | TEM EDS, SAED | Tomeoka et al. 2008 |
| Taenite | high-Ni Fe,Ni | | | | | | | X | | 24 | Bulb | TEM EDS | Leroux et al. 2008a |
| Taenite | high-Ni Fe,Ni | | | X | | | | | Assoc. w/pyrrhotite, kamacite | 51 | Transi-tion | TEM SAED | Leroux et al. 2008a |
| Taenite | high-Ni Fe,Ni | X1 | X | | | | | | Assoc. w/kamacite, pyrrhotite, low-Ca px | 62 | TP1Sub trackI | SXRD and microtomography | Nakamura et al. 2008a |
| Fe-Ni metal (unspecified) | Fe,Ni | | | | X | | | | | 16 | Bulb | TEM EDS, EFTEM | Leroux et al. 2008a |

The few exceptions are Mg in grain 51 and 42; Fe in grain 51; and S in grains 16 and 51. Most of the variation in grain 51 is due to a single extreme analysis. Adjacent grains have very different analytical ranges and means (Figs. 6–11). For example, Mg, Ca, and S are much more abundant in all analyses from grain 24 than in nearby grain 16. Similarly, Mg is more abundant and Fe and S less abundant in all (save one extreme) analyses from grain 52 than in nearby grain 51.

## DISCUSSION

All melted grains from Track 35 examined in this study consist largely of a texturally and compositionally heterogeneous emulsion of immiscible metal/sulfide beads nanometers to tens of nanometers in diameter in a silica-rich vesicular glassy amorphous material, identical to common Stardust material as described by Zolensky et al. (2006, Figs. 1A and B), Leroux et al. (2008a, 2009), and Tomeoka et al. (2008) and similar to known silicate-dominated shock melts with quenched metal-sulfide objects in ordinary chondrites (Leroux et al. 2000).

### Nature of the Incident Comet-Dust Particle that Formed Track 35

Curatorial notes indicate that the terminal particle of Track 35's single main stylus (58, an optically transparent object, probably consisting predominantly or exclusively of crystalline silicate) and the three nearest objects (including 57, an optically opaque object) were lost during sample processing. Consequently, it is not known what sort of crystalline terminal particle(s) are associated with the melted grains examined here. However, using synchrotron methods, Nakamura et al. (2008a) examined five grains from the bulb and stylus portions of Track 35 that contained crystalline phases (three consisting dominantly of crystalline silicates and two more consisting primarily of Mg- and Si-rich amorphous material containing crystalline metals and sulfides). Two of these grains were terminal particles of short subsidiary styli ("subtracks"); grain 6 was a chondrule-like microrock that contained kamacite (see also Nakamura et al. 2008b), and grain 62 was mostly amorphous with crystalline kamacite and sulfides (Nakamura et al. 2008a, Table 1 and Fig. 1). Crystalline phases identified from synchrotron X-ray diffraction data in the grains classified as crystalline include Mg-rich olivine, Ca-poor pyroxene, Ca-rich pyroxene, plagioclase and kamacite. Several of the crystalline grains briefly described by Nakamura et al. (2008a)—grains 4 and 6—are further described as chondrule-like by Nakamura et al. 2008b, based on mineral assemblages, textures, and oxygen isotope systematics very similar to those of carbonaceous chondrites. These apparently unmodified surviving fragments of the incident comet-dust particle indicate that it included chondrules of carbonaceous-chondrite-like character.

The occurrence of these chondrule-like microrocks in Track 35 also indicates that the numerous melted grains in Track 35 are a preferentially melted fraction of a fragile, heterogeneous incident particle. Preferential melting of a fine-grained fraction (relative to survival of coarser-grained fractions) is a parsimonious interpretation of the properties of the melted grains (Leroux et al. 2008a; Roskosz et al. 2008). The compositional average for the five allocations suggests broadly chondritic ratios of elements indigenous to the cometary particles (Table 3). Chondrule-like objects with carbonaceous chondrite oxygen isotopes (Nakamura et al. 2008b) coexisted with fine-grained material of CI bulk composition (that preferentially melted and then quenched to form the melted glassy grains; Leroux et al. 2008a; Roskosz et al. 2008) in the incident comet-dust particle that formed Track 35.

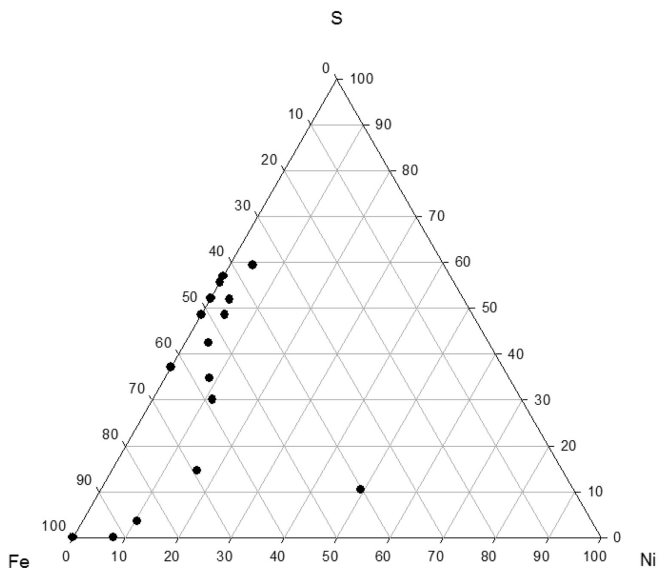


Fig. 2. Compositions (atom%) of sulfide/metal grains from grain 16 plotted on an Fe-Ni-S ternary. Spot analyses include spots from within a euhedral crystal, an angular grain, multiple individual beads, and multiple spots on a compound bead.

### Distribution of Sulfide and Metal Phases in Beads within Melted Grains in Track 35

Specific minerals in Fe-Ni-S system identified to date in microrocks, angular grains, and beads by previous work on Stardust grains from other tracks, and from Track 35, are summarized in Table 2. They include: Fe,Ni metal (mainly kamacite, some taenite), sulfide (Fe-monosulfides, pyrrhotite and/or troilite; (Fe,Ni)S, pentlandite), and mixed multiple-sulfide and metal-sulfide grains (Zolensky et al. 2006, 2008b; Brownlee et al. 2006; Leroux et al. 2008a; Nakamura et al. 2008a, 2008b; Tomeoka et al. 2008). Large-area TEM-EDS analyses for the five grains from Track 35 examined here suggest that Fe and S are correlated (Fig. 6), and that Fe/S ratios (average 0.89) in the bulb of the aerogel capture track nearest the entry aperture (Fig. 10) are consistent with an iron

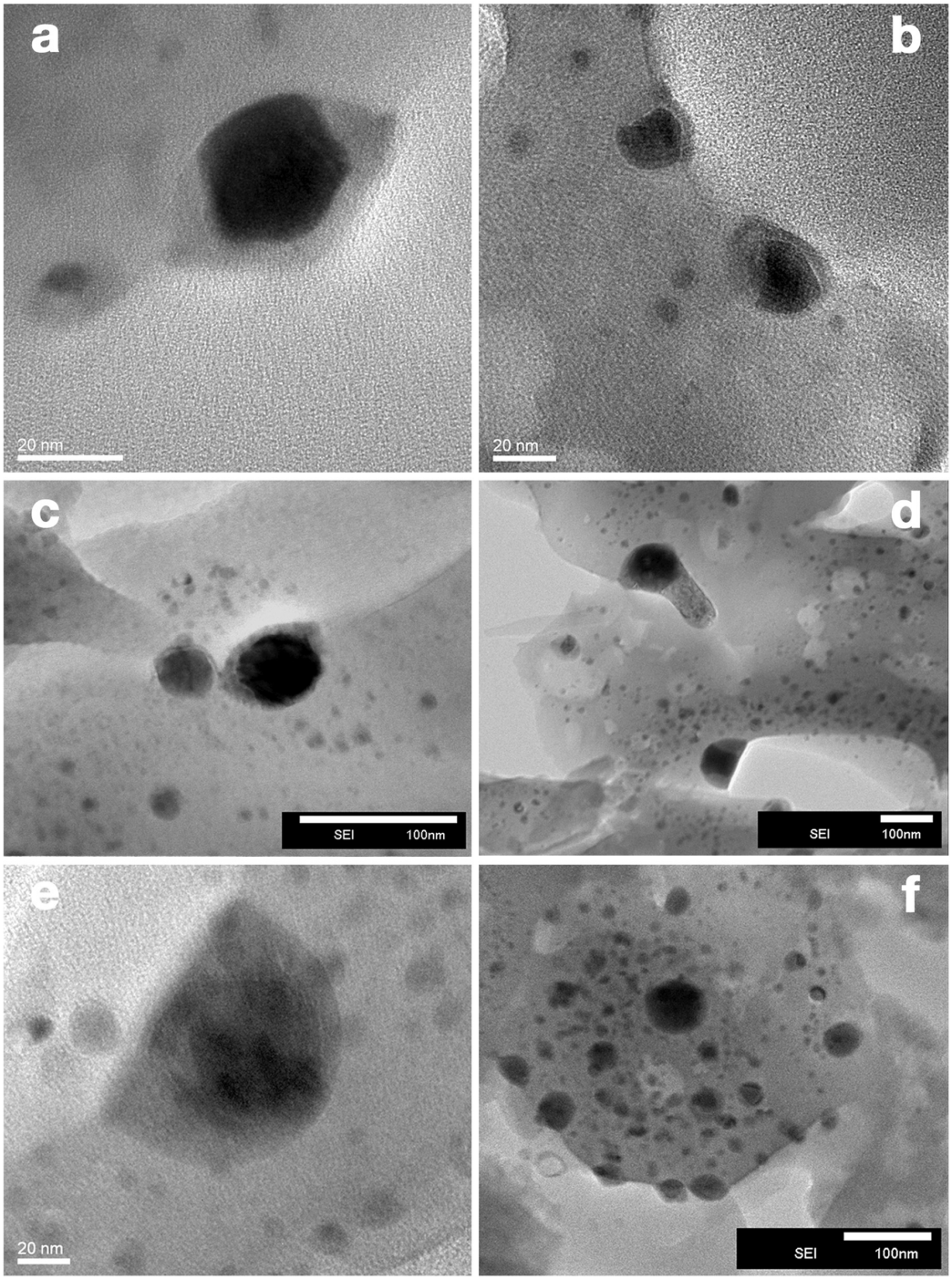


Fig. 3. Non-spherically symmetric metal-sulfide droplets distributed as lenses with long axes aligned along interface between amorphous silica-rich glass (with metal/sulfide droplets) and vesicles. a) Metal-sulfide lens at nearly straight interface between silica-rich glass (darker, upper left) and (empty) vesicle (lighter, lower right). TEM image, grain C2054,0,35,16,8, slice #40. b) Metal-sulfide lenses at gently concave interface between silica-rich glass (darker, lower left) and (empty) vesicle (lighter, upper right). TEM image, grain C2054,0,35,16,8, slice #40. c) Metal-sulfide lenses at gently concave interface between silica-rich glass (darker, below) and (empty) vesicle (lighter, above). STEM image, C2054,0,35,24,8, slice #34. d) Non-spherically-symmetric metal-sulfide droplets. Upper object has spherically symmetric core but elongate shell. Lower object occurs as a lens at a strongly concave interface between silica-rich glass and the end of an elongate empty vesicle. STEM image, C2054,0,35,42,3, slice #11. e) Metal-sulfide lens at concave interface between silica-rich glass (darker, lower right) and (empty) vesicle (lighter, upper left). TEM image, C2054,0,35,52,6, slice #26. f) Globular GEMS-like object consisting of silica-rich glassy material densely decorated by metal/sulfide droplets. The GEMS-like object is roughly spherical in outline, and is bounded by an empty vesicle at the bottom of the image. All metal-sulfide objects on the globule-vesicle interface (seen tangentially to the spherical surface) are lenses elongate along the globule's convex surface. STEM image, C2054,0,35,42,3 slice #12.

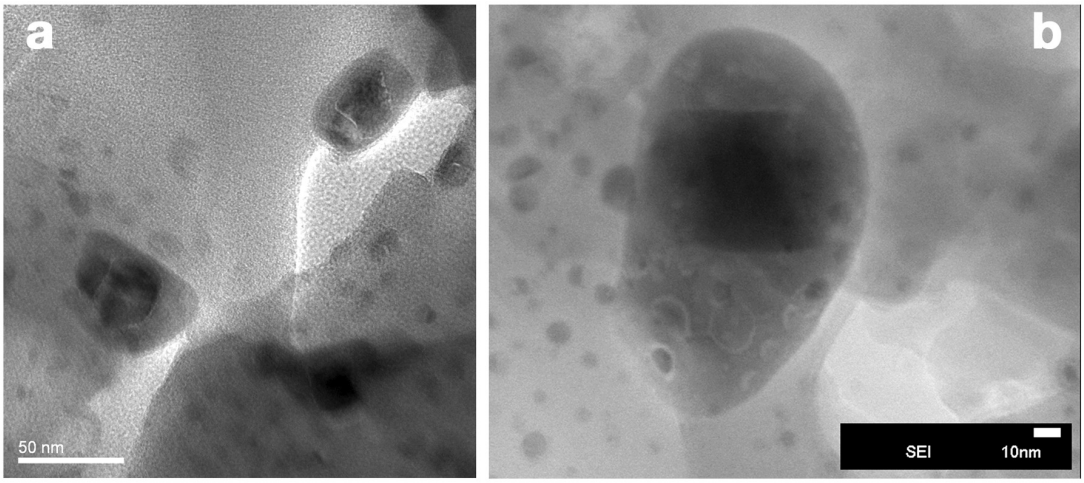


Fig. 4. Beads with cores and rims that are not spherically symmetric. a) Non-spherical metal core with conforming shell. TEM image, C2054,0,35,16,8 slice #40. b) Non-spherical metal core with non-conforming smooth shell. STEM image, C2054,0,35,42,3, slice #12.

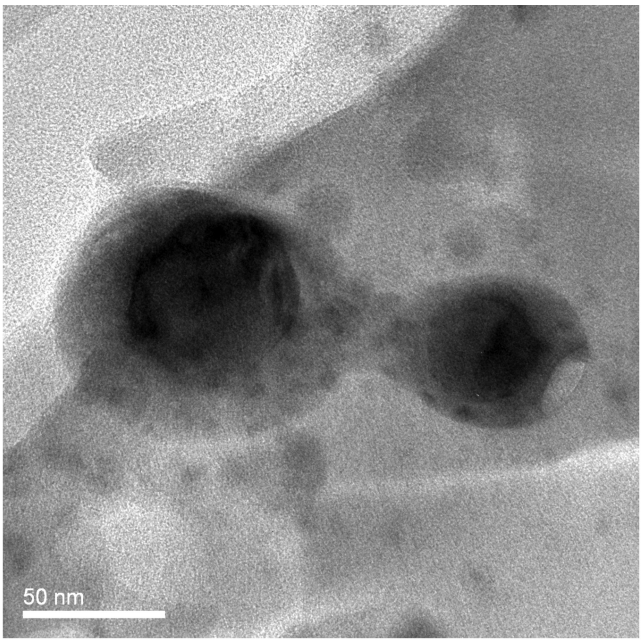


Fig. 5. TEM image of a pair of concentrically layered objects consisting of two discrete metal cores joined by a filament or "bridge" of shell material. C2054,0,35,16,8 slice #37.

monosulfide mineral. The compositions of individual metal-sulfide beads and compositionally similar angular grains we observe in grain 16 (Fig. 2) are very similar in distribution and range to those previously reported from a different allocation of the same grain by Tomeoka et al. (2008), and by Leroux et al. (2008a) from nearby grain 24 in the same track. All these sets of analyses from grains 16 and 24 in this track contain individual spot analyses with higher Ni contents than reported from the overall population of all Stardust grains examined during the preliminary examination stage (Zolensky et al. 2006, 2008b) or from any other individual grains (Leroux et al. 2008a; Tomeoka et al. 2008). Track 35 appears to be unique among Stardust materials described to date in containing such high-Ni inclusions.

Table 3. Elemental abundances (atom%) from large areas, analyzed by TEM-EDS (Si & O excluded).

| Grain | Mg | Fe | Ni | S | Ca | Cr |
|---|---|---|---|---|---|---|
| 16 | 37.29 | 24.93 | 2.47 | 31.40 | 2.80 | 1.11 |
| 24 | 46.80 | 19.05 | 1.34 | 19.56 | 12.28 | 0.97 |
| 42 | 36.62 | 37.72 | 2.11 | 19.29 | 1.83 | 2.44 |
| 51 | 38.14 | 32.73 | 1.64 | 24.59 | 1.90 | 1.00 |
| 52 | 48.74 | 29.02 | 2.38 | 17.87 | 1.18 | 0.81 |
| Average | 41.52 | 28.69 | 1.99 | 22.54 | 4.00 | 1.27 |
| CI (Leroux et al. 2008a) | 38.0 | 32.0 | 1.7 | 18.0 | 2.1 | 0.5 |

## Morphology of Beads: Solidified, Formerly Melted Droplets

Melting (Zolensky et al. 2006) and/or vaporization and condensation (Leroux et al. 2008a, 2009), followed by cooling, are the most likely processes relating the observed Fe-Ni-S minerals to one another and determining their textural relationships. Whether the beads formed by melting or vaporization/condensation, completely molten droplets in free-fall would take on a spherical (surface-tension controlled) geometry in the absence of other forces (Leroux et al. 2008a). The distribution of metal cores and sulfide shells within beads formed by complete melting is consistent with expected immiscibility between sulfide and metal melts; similarly, the surface-tension-controlled shapes of the metal/sulfide droplets embedded in silica-rich material is consistent with expected silicate/metal-sulfide immiscibility (Leroux et al. 2008a). Sulfide/metal beads are presently interpreted as solidified droplets of once-molten material,

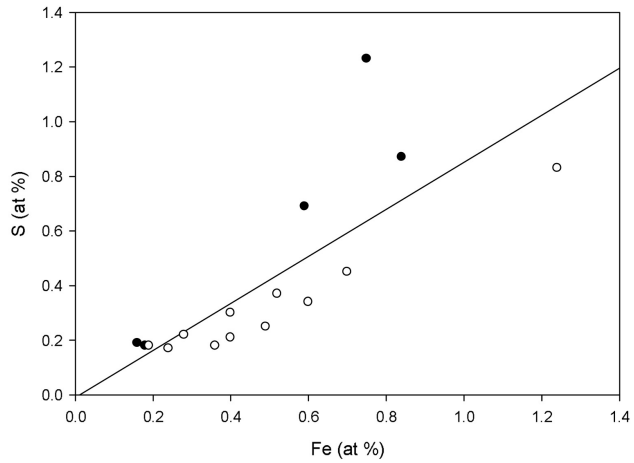


Fig. 6. Fe versus S (atom%) in whole-area TEM-EDS analyses. The slope is 0.86, indicating on average less S than present in stoichiometric iron monosulfide; $r^2$ = 0.63. All analyses plotted above the regression line (higher S/Fe ratio than the regression line) with at% S > 0.6 are from melted grain 16, in the bulb portion of Track 35. All but one of the analyses plotted above the regression line are from the bulb (grains 16 and 24; filled circles); all but one of the analyses plotted below the regression line (lower S/Fe ratio than the regression line) are from farther down-track (open circles), in the bulb-stylus transition (grains 51 and 52) or in the stylus (grain 42). Melted grains farther down-track than the bulb have consistently lower S/Fe ratios than melted grains in the bulb.

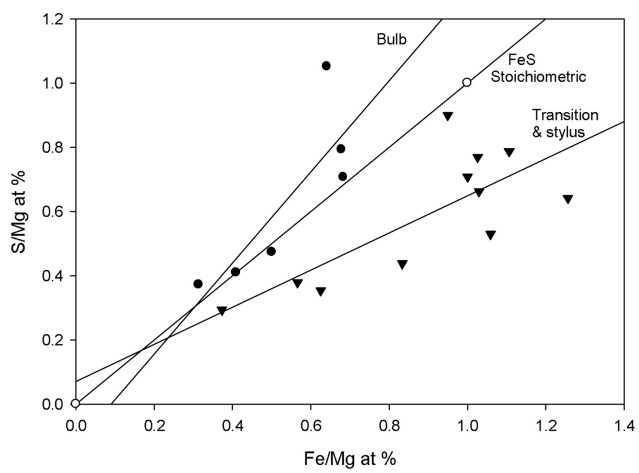


Fig. 7. S/Mg atomic ratio as a function of the Fe/Mg atomic ratio from whole-area TEM-EDS analyses for melted grains in the bulb (grains 16 and 24; filled circles) and from farther down-track (inverted triangles), in the bulb-stylus transition (grains 51 and 52) and in the stylus (grain 42). The linear regression line for the melted grains from the bulb has a slope of 1.42, a negative y-intercept, and $r^2$ = 0.69; the linear regression line for the melted grains from the bulb-stylus transition and the stylus has a slope of 0.58, a y-intercept of 0.07, and $r^2$ = 0.59. Also shown for comparison is the slope for stoichiometric FeS (open circles). See text for discussion.

heated to melting by the conversion of kinetic energy to heat during rapid deceleration of the cometary particle as it penetrated the aerogel (Leroux et al. 2008a, 2009).

Deviations from simple spherical geometry, although

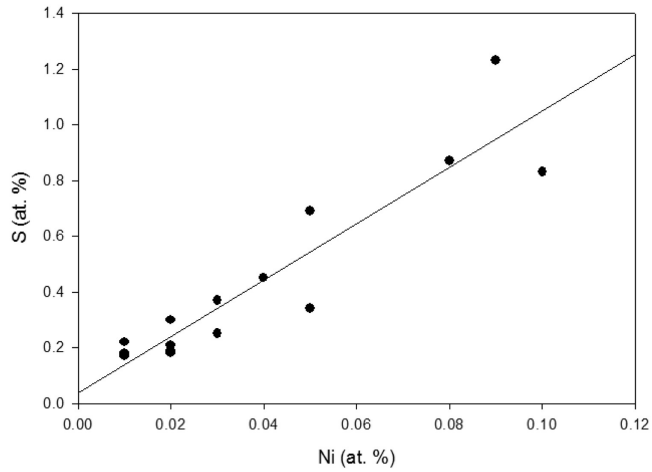


Fig. 8. Ni versus S (atom%) in whole-area TEM-EDS analyses; $r^2$ = 0.85.

relatively uncommon as a fraction of all occurrences, might be especially informative (Leroux et al. 2008a). Steady state deformation of drops is influenced by external forces (acting against viscosity) that tend to deform, disrupt and even break the drop, and interfacial forces that tend to restore the undeformed shape (Fischer and Erni 2007), but non-spherical Stardust droplets are likely not equilibrium or steady-state shapes. Quantitative analysis of drop shape must invoke boundary conditions more complex than steady relative flow of drops and host phase, incompressible fluids, negligible inertia and buoyancy (Stone 1994; Fischer and Erni 2007) in order to apply to the short-lived, transient Stardust capture-melts. Beads with highly irregular margins might represent juxtaposition of localized melts of different compositions, with different interfacial energies and surface tensions than the more common melts that solidify with more regular margins (Leroux et al. 2008a).

### *Lens-Shaped Beads at Glass-Vesicle Interfaces*

One recurring non-spherical variant is the metal-sulfide lenses at the interface between sulfide-bearing silica-rich glass and (empty) vesicles (Fig. 3; see also Fig. 11d in Leroux et al. 2008a). Lenticular two-phase beads were observed in all five allocations examined for this study, from all penetration distances along Track 35; Fig. 3 shows examples from four of the five allocations. These lenses are elongate with their long axes aligned along the interface (Fig. 3). This suggests a geometry controlled by surface tension acting on a minor phase distributed discontinuously along the interface between a compositionally different volumetrically dominant phase and a vesicle (Leroux et al. 2008a). Lenses extend more deeply into the silica-rich glass than into the vesicles, regardless of the curvature of the glass-vesicle interface (Fig. 3), suggesting systematic differences between the sulfide-glass and sulfide-vapor interfacial tensions. This is true even for the convex surfaces of globular silica-rich

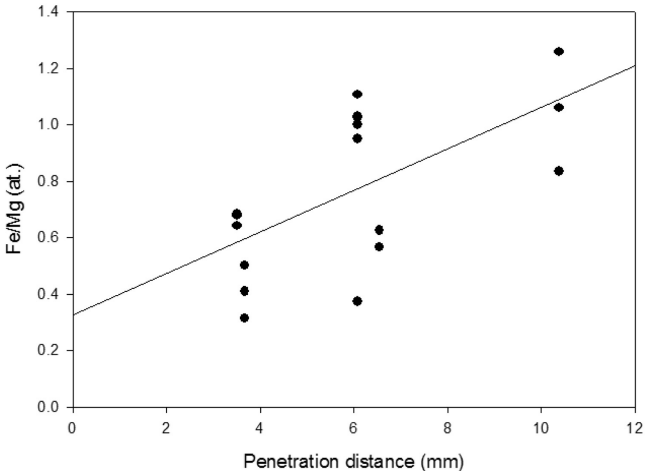


Fig. 9. Fe/Mg (atom proportions) as a function of grain penetration distance into aerogel along Track 35; $r^2 = 0.38$.

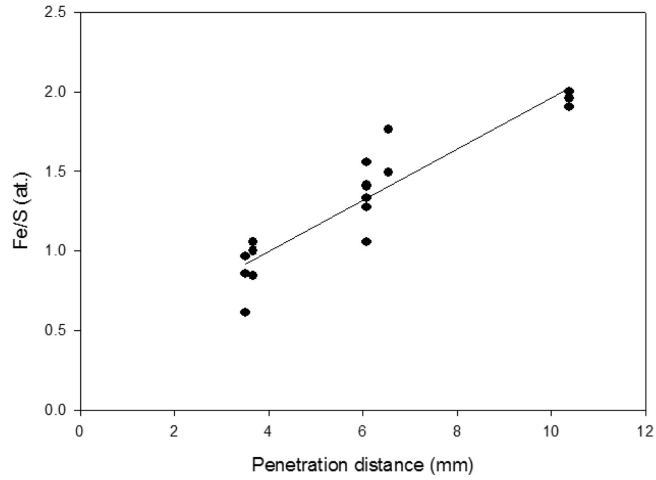


Fig. 10. Fe/S (atom proportions) as a function of grain penetration distance into aerogel along Track 35; $r^2 = 0.85$. Total length of Track 35 is 11.7 mm. Note that Fe/S ratios are near unity in the allocations from the bulb (near 4 mm penetration depth), increase substantially in the bulb-stylus transition (6–7 mm penetration depth) and are highest far along the stylus (~11 mm penetration depth) near the terminal particle.

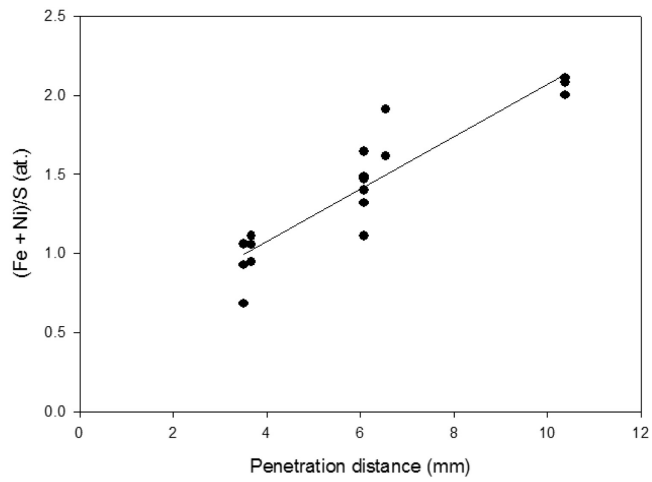


Fig. 11. (Fe + Ni)/S (atom proportions) as a function of grain penetration distance into aerogel along Track 35; $r^2 = 0.84$.

objects (Fig. 3f) that resemble GEMS (glass with embedded metal and sulfides; Bradley 1988) but occur in melted Stardust grains (Zolensky et al. 2006; Ishii et al. 2008a; Tomeoka et al. 2008). This interfacial texture may help distinguish aerogel-capture melt globules in melted Stardust materials from true GEMS (supporting preliminary textural distinctions suggested by Zolensky et al. 2006, including their Figs. 1c and 1d; complementing mineralogical differences described by Ishii et al. 2008a; and supplementing compositional contrasts noted by Zolensky et al. 2006 and Ishii et al. 2008a).

The physics of liquid lenses or drops of immiscible third phases (in this case, two-phase beads) at a two-phase interface (in this case, the wall of the vesicle in the predominantly silicate melt) are well understood in the classic formulations (Davies and Rideal 1963; Adamson 1990), but the Stardust materials introduce several additional complexities. Conventional treatments are for three-phase systems (a host liquid, an overlying phase such as air, and an immiscible liquid distributed as lenses along the otherwise planar host-liquid/vapor interface), whereas the Stardust textures involve four immiscible fluids (molten silicate, molten metal, molten sulfide, and vapor forming the vesicles). Unlike the conventional formulation for treatments of immiscible lenses at interfaces, the metal-sulfide beads in Stardust grains are themselves two-phase objects (Fig. 3), consisting of metallic and/or Ni-rich cores and Ni-poor sulfide shells. When distributed along a vesicle wall, the shape of such lenses will be influenced not only by sulfide-melt/silicate-melt and sulfide-melt/vapor interfacial tensions, but also by rheologic and viscosity contrasts between the sulfide and Ni-rich/metal phases within the liquid lenses. Furthermore, many occurrences of immiscible metal-sulfide lenses in Stardust melted grains are along curved vesicle walls rather planar silicate-vapor interfaces (e.g., Fig. 3d, lower right). Consequently, the apparent wetting angles measurable from TEM images (Fig. 3) will be influenced by a variety of geometric and fluid-mechanical factors beyond those standard to the study of three-phase interfacial phenomena (Davies and Rideal 1963; Adamson 1990).

### *Beads with Non-Spherical Cores*

In some beads with cores and distinct shells of largely uniform thickness, the cores are not spherical but instead subangular, with rounded corners (Fig. 4). This geometry is difficult to explain as a surface-tension controlled form taken on by a fully molten compositionally homogeneous metal core. This suggests the possibility of incomplete melting of a precursor (metal) mineral still preserved as the core. Equant

but initially angular grains become rounded (beginning with rounding of edges and corners) if mass- or heat-transfer is rate-determining during dissolution or melting (Velbel 2004). This core morphology suggests that some bead/droplet precursors were not completely melted during particle capture. If so, core minerals in such objects may be relict cometary minerals and not products of melting during aerogel capture, and such examples may be exceptions to the model of Leroux et al. (2009) according to which metal cores of beads formed by reduction of originally silicate-hosted Fe.

Leroux et al. (2008a, their Fig. 10) describe an uncommon metal-sulfide object from grain 51 in Track 35, in which a rounded but not spherical core (surrounded by a pyrrhotite rim) contains two discrete bulbous volumes, one each of kamacite and taenite. This is not an obvious subsolidus exsolution texture; it is unclear whether it is inherited from an incompletely melted incident metallic mineral, produced during cooling a fully molten metal droplet, or formed by some other means.

### *Compound Beads*

Compound beads (Fig. 5) consist of pairs of Fe-Ni-rich cores connected to one another by bridging material consisting of Fe-S-rich material. Such "dumbbell" shaped objects strongly resemble the shapes taken by rotating drops of liquids in free-fall, as demonstrated on Skylab (Summerlin 1977). Figure 5 shows a compound bead in which the two lobes are arranged in a manner identical to fast-spinning liquid drops in free fall just below the spin-rate threshold at which the mass of liquid fissions into two discrete drops (Summerlin 1977). Leroux et al. (2008a, Fig. 11c) describe a compound droplet, the shape of which indicates incomplete breakage of a larger drop disrupted by translational and rotational motion of the breaking drop through molten aerogel. Leroux et al. (2008a, Fig. 11b) describe another complex bead in which the core is elongated between the two lobes of a dumbbell shaped envelope. They attribute this texture to coalescence of the two drops and solidification prior to acquisition of an equilibrium shape (a plausible explanation for other occurrences of broadly similar textures in other less dynamic settings; e.g., Leroux et al. 2003). An alternative interpretation is that this object solidified from a rapidly spinning droplet, the core of which has not yet separated into two discrete cores. Interestingly, no Stardust sulfide/metal beads have yet been observed with textures resembling those of coalescing drops in free fall (Summerlin 1977). These observations suggest that fissioning of rapidly spinning melt droplets during aerogel capture is a more likely explanation than coalescence for these Stardust compound bead textures. In addition, these compound beads indicate that, if Fe metal droplets formed by high-temperature reduction of silicate-hosted Fe and the Fe-sulfide shells formed subsequently by oxidation of Fe and reduction of S previously volatilized during heating (the preferred model of Leroux et al. 2009), both phases in the two-phase assemblages were still molten, in motion, and deforming as two-phase droplets throughout the oxidation-sulfidation stage of the process.

## Multiple Origins of Phases in the System Fe-Ni-S

Zolensky et al. (2006) reported that sulfides and Fe-Ni metal occurred as parts of melted grains and as unmodified minerals in indigenous cometary particles. However, they did not elaborate upon detailed criteria for the proposed distinction. Subsequent work has started to fill in this gap. Pyrrhotite, pentlandite, kamacite and taenite have all been identified by TEM or SXRD in microrocks that were apparently not thermally modified during aerogel capture (Table 2; Brownlee et al. 2006; Zolensky et al. 2006; Nakamura et al. 2008a, 2008b). Thus, all these minerals were part of the mineral inventory of comet 81P/Wild 2 dust prior to capture in aerogel. Pyrrhotite, kamacite and taenite (but not pentlandite) have been reported from capture-melted Stardust grains, almost always as part of metal-sulfide beads that likely formed predominantly by quenching of immiscible metal-sulfide droplets dispersed in silica-rich melt (Table 2; Rietmeijer et al. 2008; Zolensky et al. 2008b; Leroux et al. 2008a; Tomeoka et al. 2008). However, as noted in the section on bead textures above, some incompletely melted cometary metal may persist in the cores of some otherwise molten beads. Thus, most metal and sulfide minerals can occur as preserved indigenous cometary minerals (in capture-unmelted microrocks), as products of complete melting and crystallization during quenching of metal-sulfide beads (and therefore not part of the incident cometary particle's mineral inventory), or as incompletely melted relict cometary minerals in metal-sulfide beads. The following paragraphs evaluate the evidence for the possible origins of each previously reported metal and sulfide mineral.

### *Low-Ni Minerals: Kamacite and Pyrrhotite*

In Track 35, metallic Fe-Ni (kamacite) occurs (Table 2) both (1) as a cometary mineral enclosed within an olivine crystal in a porphyritic-chondrule-like polycrystalline grain (microrock) unmodified by aerogel capture (Nakamura et al. 2008a, 2008b), and (2) in capture-modified grains, where Ni-rich metal inferred to be taenite also occurs (Nakamura et al. 2008a; Tomeoka et al. 2008). Kamacite in an unmodified microrock (grain 6; Nakamura et al. 2008a, 2008b) indicates that Fe-Ni metal was present in the incident comet-dust particle that produced Track 35.

In Track 35, crystalline kamacite occurs (along with pyrrhotite, taenite, and possibly troilite) in a few of the grains classified as amorphous (Nakamura et al. 2008a; suessite and metallic tungsten were also identified, but are probably not cometary phases). Kamacite in melted grains may therefore

be either a relict (unmelted) cometary mineral or a product of melting and solidification during aerogel capture.

Pyrrhotite, kamacite and taenite (but not pentlandite) have been reported from capture-melted Stardust grains, almost always as part of metal-sulfide beads that likely formed predominantly by quenching of immiscible metal-sulfide droplets dispersed in silica-rich melt (Table 2; Rietmeijer et al. 2008; Zolensky et al. 2008b; Leroux et al. 2008a; Tomeoka et al. 2008). The ubiquity of Ni-bearing cores in, and Fe-sulfide shells on, large core-mantle beads, and the crystallographic identification of kamacite and pyrrhotite in multiple occurrences of each type, suggest that kamacite and pyrrhotite form during the capture-melting process. Thus, pyrrhotite and kamacite can occur both as unmodified comet minerals and as products of aerogel-capture melting and quenching.

### *High-Ni Minerals: Taenite and Pentlandite*

Although taenite occurs in both unmelted (Table 2; Brownlee et al. 2006; Zolensky et al. 2006; Nakamura et al. 2008a) and melted (Table 2: Rietmeijer et al. 2008; Zolensky et al. 2008b; Leroux et al. 2008a; Tomeoka et al. 2008) grains, all documented occurrences of taenite are from a single track (Track 35), so additional scrutiny of the evidence is required before inferences can be drawn about modes of taenite formation. Occurrence of taenite in unmelted grains (Table 2; Brownlee et al. 2006; Zolensky et al. 2006; Nakamura et al. 2008a) is evidence for the occurrence of taenite in comet dust before capture.

The matter of whether taenite also forms during aerogel capture is less clear. EDS analyses of Fe-Ni-S-bearing objects in grains 16 (Fig. 2) and 24 (many low-S, high-Ni spots) are similar to each other but different from those in grain 51 (all low-Ni) (Leroux et al. 2008a, their Fig. 12b; Tomeoka et al. 2008, their Fig. 6b). The low-S, high-Ni EDS analyses from grains 16 and 24 could be due to the presence of taenite or S-depleted pentlandite, or both (Leroux et al. 2008a, their Fig. 12b; Tomeoka et al. 2008, their Fig. 6b). Taenite has not been reported to date as occurring in any grain from any Stardust track other than Track 35. However, taenite has been identified by TEM SAED in another allocation from (melted) grain 16 from the bulb portion of Track 35 (Tomeoka et al. 2008, p. 282), and inferred to occur in nearby (melted) grain 24 on the basis of that grain's high Ni content as measured by TEM EDS (Leroux et al. 2008a, p. 114). Taenite has also been identified in two other grains from Track 35; by TEM SAED of grain 51, from the bulb-stylus transition region (Leroux et al. 2008a); and by SXRD of grain 62, the terminal particle of a small branching subtrack (Nakamura et al. 2008a). Both down-track taenites are in grains associated with other minerals. In grain 62, taenite occurs with kamacite, pyrrhotite, and low-Ca pyroxene in a terminal particle from a branching subtrack (Nakamura et al. 2008a, their Fig. 6). Survival of pyroxene in grain 62 suggests the grain was not completely melted during aerogel capture; in extensively melted grains, the former presence of pyroxenes or olivines is indicated by compositional heterogeneity in glass, not by persistence of the silicate mineral itself (Leroux et al. 2008a; Roskosz et al. 2008). In grain 51 (from the bulb-stylus transition area), taenite occurs along with kamacite and pyrrhotite in a morphologically complex partially angular, possibly subhedral object with an unusual bulbous metal core (Leroux et al. 2008a, their Fig. 10). In neither downtrack occurrence does petrographic evidence distinguish possible capture-related melting and crystallization from possible preservation of precapture crystallization textures.

Existing published data favor the interpretation that taenite is the host phase for Ni in Ni-rich grains 16 and 24 near one another in the bulb of Track 35. Published data further indicate that taenite also occurs farther downtrack in Track 35. The observation that taenite is the one mineral in the system Fe-Ni-S that has not been reported in any other Stardust track militates against the hypothesis that taenite forms during aerogel-capture melting of projectile minerals. This suggests that taenite in any individual Track 35 grain is either preserved, unmodified cometary taenite, or Ni-rich metal formed by capture melting in Track 35 because of the presence of unusually Ni-rich incident comet dust in the particle that formed Track 35.

Nickel-bearing sulfides (pentlandite) have been documented from Stardust grains, but are not common (one occurrence each from Tracks 10, 27 and 59; Brownlee et al. 2006; Zolensky et al. 2006, 2008b). In general, Ni contents of Stardust sulfides are comparable to sulfides in anhydrous interplanetary dust particles (IDPs) and too low to map onto the population of sulfides from hydrous IDPs (Zolensky et al. 2006, Fig. 2a; 2008b; Zolensky and Thomas 1995; Dai and Bradley 2001). Pentlandite has not been reported to date from any allocation of Track 35. However, (melted) grain 24 from Track 35 is notably rich in Ni among the many allocations examined by Leroux et al. (2008a), and the unique role of taenite as a Ni host-phase in Track 35 has been noted (above). In other tracks, Ni and S are uncorrelated or even negatively correlated, suggesting that Ni is associated with olivine rather than sulfides (Lanzirotti et al. 2008). However, in the allocations from Track 35 examined here, Ni is positively correlated with S (Fig. 8), suggesting that either Ni is sulfide-hosted in Track 35, or that S is spatially associated with another, Ni-rich phase (for example, S in Fe-monosulfide shells surrounding Ni-rich Fe-metal cores). Nickel is likely hosted by different minerals in different tracks, depending upon differences in mineral composition of different incident comet-dust particles. The documented high Ni abundance and multiple occurrence of taenite in Track 35 all suggest that, among all Stardust grains examined to date, those from Track 35 warrant further study for insight into distinguishing pre-capture from capture-modified Ni host minerals.

## Bulk Compositions of Melted Grains, and Along-Track Variation

The compositional average for the five allocations suggests broadly chondritic ratios of elements indigenous to the cometary particles (Table 3), consistent with previous studies of the bulk composition of melted grains (e.g., Leroux et al. 2008a). The largest relative deviation of average melted-grain analyses from Track 35 and CI is for Cr (~2.5 times CI), which is known to be heterogeneously distributed along Stardust tracks, presumably because of heterogeneous distribution of the Cr host mineral in the incident particle and its fragments (Flynn et al. 2006; Flynn 2008). The ensemble of melted grains from Track 35 analyzed for this study, taken together, indicate a relatively simple and familiar carbonaceous-chondrite-like compositional character to the pre-capture material that became the melted grains, as previously inferred from other studies of melted grains (Leroux et al. 2008a), and similar to the overall compositional inferences based on aggregated data from melted and unmelted grains (Flynn et al. 2006). However, individual melted grains, and within-grain and between-grain variations in composition, provide additional insight into the nature of the pre-capture comet dust and the capture-melting process.

Previous work has demonstrated spatially heterogeneous distributions of major elements within individual extensively melted Stardust grains (Leroux et al. 2008a; Lanzirotti et al. 2008; Tomeoka et al. 2008; Stephan et al. 2008; Roskosz et al. 2008). Composition varies between different grains that came to rest near one another. Grain 16 has lower Mg and Ca and higher S abundances than nearby grain 24 (Table 3). These two grains are similar to one another, and different from most other grains from Track 35, in having large numbers of objects that yield S-poor, Ni-rich (taenite-like and/or S-depleted pentlandite) TEM-EDS analyses (Fig. 2; see also Leroux et al. 2008a, Fig. 12b; Tomeoka et al. 2008, Fig. 6b). Similarly, grain 52 has higher Mg, and lower Fe and S abundances that nearby grain 51 (Fig. 9; Table 3; nearly identical compositions were reported for other allocations of grains 51 and 52 by Leroux et al. 2009). This suggests that different pre-melted comet dust fragments had different abundances and compositions of silicate and sulfide minerals in different ~10 micron fragments, that upon melting produced different silicate-glass compositions in adjacent grains at similar positions along the aerogel capture track. Bulk-compositional and textural attributes of ~10 micron-scale melted grains were largely controlled by the compositional heterogeneity between different ~10 micron-scale fragments of the incident comet dust. This is consistent with the observations and inferences of Leroux et al. (2008a), Lanzirotti et al. (2008), Tomeoka et al. (2008), and Stephan et al. (2008).

Against a backdrop of modest compositional heterogeneity within individual slices (Leroux et al. 2008a; Lanzirotti et al. 2008; Tomeoka et al. 2008; Stephan et al. 2008), and considerable compositional variation between grains at the same penetration distance along the aerogel track (Figs. 9–11), some element ratios vary systematically along the track. Fe/Mg (Fig. 9), Fe/S (Fig. 10), and (Fe + Ni)/S (Fig. 11) increase with distance from the entry aperture. The next paragraphs discuss the significance of these along-track compositional variations. If Fe loss occurred as proposed by Stephan (2008) and Flynn (2008), many of the trends discussed below (e.g., S loss) are even more pronounced.

### *Density Sorting*

All the melted grains with the highest Fe/Mg ratios (e.g., greater than 0.70) are from the beyond the bulb (in the bulb-stylus transition or in the stylus), all bulb grains have Fe/Mg less than 0.70, and barely one-fourth of the down-track melted grains have Fe/Mg below 0.70 (Figs. 7, 9). Our results for along-track variations in Fe/Mg are consistent with the recently published work of Stephan et al. (2008) on the same Stardust aerogel-capture track. Grain 45, from the stylus portion of Track 35 very near grain 42 examined in this study, has the highest Fe/Mg ratio of all grains Stephan et al. (2008) examined, including three others from Track 35. Magnesium-rich grains are found in the bulb of Track 35, while both grains in the stylus near the track terminus have high Fe abundances (Stephan et al. 2008).

Along-track variations in composition may be due to size- and/or density sorting during aerogel capture. Table 3 shows that the average compositions of the five allocations examined here have systematically higher Fe abundances with increasing penetration distance along Track 35. As a percentage of the indigenous elements not introduced by mixing with aerogel (Mg, Fe, Ni, S, Ca, Cr), the two melted grains from the bulb (grains 16 and 24) both have well below-average and below-CI Fe abundances (between 19–25%); the two melted grains from the bulb-stylus transition (grains 51 and 52, grains from which other allocations were analyzed by Leroux et al. 2008a, and Leroux et al. 2009) have near-average and near-CI Fe abundances (between 29–33%); and the melted grain farthest down-track (grain 42) has well-above average and above-CI Fe (nearly 38%). The deepest-penetrated melted grain thus contains up to twice as much Fe as the melted grains that penetrated only as far as the bulb of the capture track. Other abundant heavy elements vary much less among different allocations (Ni, 1.3–2.5%; Cr, 0.8–2.5%), leaving the large differences in Fe abundance as the main compositional influence on the density of the melted grains.

Penetration depths of micron-scale particles into soft targets (e.g., animal tissue) increase with increasing particle density, radius, and velocity (Mitchell et al. 2003). All 81P/Wild 2 comet-dust particles entered the Stardust aerogel at identical incident (initial) velocities, but impact-disrupted fragments leave the impact site with a range of velocities. During explosive fragmentation of uniformly dense material,

larger fragments have faster velocities (Curran 1997). Besides velocity, fragment size and density are the main remaining sources of variation to account for variations in penetration depth. Terminal particles in Stardust aerogel are typically microns in size, leading Zolensky et al. (2008b) to suggest that disruption of texturally heterogeneous comet dust results in larger fragments penetrating deeper into aerogel. Assuming Fe-rich fragments were somewhat denser than Fe-poor fragments the heavier Fe-rich fragments may have penetrated farther into the aerogel than fragments richer in lighter elements. Burchell et al. (1999) found that iron projectiles penetrated nearly twice as far into aerogel as glass or olivine projectiles of the same particle size fired at the same velocity. Disruption of variably dense material likely results in higher velocities and consequently deeper penetration into aerogel for denser as well as larger fragments. This density-sorting process may contribute to along-track variation in Fe/Mg of melted grains in Track 35 (Fig. 9; Stephan et al. 2008).

### *Sulfur Mobilization*

The apparent decrease of S relative to Fe (Figs. 6, 7, and 10) and Ni (Fig. 11) along Track 35 supports several previously published inferences. In carbonaceous chondrite-like materials, sulfur may be initially present as Fe,Ni-sulfides, S-bearing organic compounds, or native sulfur; Fe/S ratios are near unity (ave. 0.89) in grains from the bulb of Track 35 (Fig. 10), consistent with widespread Fe-monosulfide minerals (Table 2). Combined with the observation that the Fe/Mg ratio at zero S is approximately 0.10 (Fig. 7), this also implies that very little Fe in melted Track 35 bulb grains is associated with Fe-bearing silicates or metal. This is in turn consistent with the paucity of S-free Fe-rich regions of amorphous material shown in elemental maps by Leroux et al. (2008a, 2009) and Stephan et al. (2008), in which Fe is strongly associated with S, and Mg-rich and Ca,Mg-rich amorphous materials have MgO/(MgO + FeO) near unity (Leroux et al. 2008a, 2009; Roskosz et al. 2008), suggesting origin by melting of Fe-poor silicate precursors. The (low-Fe) silicate compositions inferred from the bulb of Track 35 are also consistent with overall compositional attributes of Stardust silicates. Rietmeijer (2008) observes that, in both IDPs and Stardust allocations, Fe is hosted mainly in Fe-sulfides and to a lesser extent Fe-Ni metal, but also occurs in Mg-dominated Mg-Fe silicates. Although the population of unmelted olivines and low-Ca pyroxenes in other Stardust allocations includes some Fe-rich examples, the majority of low-Ca pyroxenes and, especially, olivines are >90% Mg and <10% Fe (Zolensky et al. 2006, 2008b).

Preservation of Fe:S stoichiometry in bulk analyses of grains 16 and 24 (Fig. 10) suggests that Fe-sulfides in the bulb were dispersed but did not lose S during formation of the bulb. This is consistent with the work of Anderson and Ahrens (1994) who suggested that fragmentation and mechanical dispersion of weak, easily fragmented grains in porous aggregates occurs under conditions of maximum stress, at the point of impact, with minimal thermal effects on the small fragments. Trucano and Grady (1995) also found that shock energy associated with the initial impact is converted primarily to deformation of the projectile and to radial kinetic energy of the fragments, rather than to shock heating. However, the grains from the bulb portion of Track 35 (grains 16 and 24) are visually identical to melted grains farther along Track 35, implying comparable (near-complete) degrees of melting in addition to mechanical disruption. Complete melting accompanied by negligible elemental redistribution has recently been reported from another bulb-sidetrack allocation, from Track 41, by Roskosz et al. (2008). Despite their extensive melting, melted grains from the bulb regions of type B (and possibly from type C) Stardust tracks may preserve indigenous compositional attributes of the incident cometary particles better than similar-looking melted grains from farther along type B tracks.

The observed along-track loss of S relative to Fe with increasing penetration distance (Fig. 10) is conspicuous in the analyses of melted grains from the bulb-stylus transition and the stylus of Track 35. Grains 51 and 52 from the bulb-stylus transition (~6 mm along Track 35) have Fe/S averaging 1.44 (our analytical results for our allocations of these two grains are indistinguishable from analyses of other allocations of the same two grains reported by Leroux et al. 2009, their Figs. 4c and 4d, which also generally show S/Fe ratios below the stoichiometric proportions for an Fe-monosulfide mineral), and the Fe/S ratio (ave. 1.95) of grain 42 (from the stylus of Track 35, ~10 mm from the entry aperture) indicates that grain 42 has only about half the S (relative to Fe) of stoichiometric Fe-monosulfides (Fig. 10). Most analyses of melted grains reported by Leroux et al. (2008a, their Fig. 6) similarly show sub-stoichiometric S/Fe ratios on a plot of Fe/Mg versus S/Mg, as do our analyses of melted grains from the bulb-stylus transition and the stylus (Fig. 7). Sulfur initially present as iron monosulfide may have been partially volatilized and redistributed during capture-melting of comet dust, as proposed by previous workers (Flynn et al. 2006; Zolensky et al. 2006; Stephan, 2008; Lanzirotti et al. 2008; Ishii et al. 2008b), leaving some of the Fe associated with remaining S in the iron sulfide shell of core-mantle beads, and the balance of the remaining Fe (now in reduced form; Leroux et al. 2008a, 2009; Rietmeijer et al. 2008) in the metallic cores of the beads (Zolensky et al. 2006, 2008b; Ishii et al. 2008a; Leroux et al. 2008a, 2009; Rietmeijer et al. 2008; Tomeoka et al. 2008). Some of the Fe remaining in the metallic cores of the beads may have originated as Fe reduced from silicates (Leroux et al. 2009). However, regardless of the original host phase(s) of the Fe, our results indicate that most S loss occurs in grains on their way out of the bulb and through the stylus (Figs. 6, 7, and 10). Although S may be volatilized upon heating and subsequently condensed as suggested by Leroux et al. (2009),

the fraction of S lost prior to condensation may vary along track. Melted grains in the bulb apparently melted and quenched under conditions that did not result in loss of volatile S, whereas melted grains farther along track in the bulb-stylus transition and the stylus appear to have lost S. Perhaps beads in melted grains in the bulb quenched more quickly, before much losing much S, in contrast to beads farther along track which, although melted to the same degree, cooled over a longer time interval and had more time to lose S which was dispersed into the surrounding aerogel.

Alternatively, the observed along-track increase in Fe over S may be a density-sorting effect (unrelated to S loss), in which grains which are more dense due to their higher Fe abundance (Stephan et al. 2008) penetrate farther into the aerogel than grains poorer in Fe (Burchell et al. 1999). Fe-Ni metal (both kamacite and taenite) has been reported in microrocks that were not thermally modified by aerogel capture (Table 2) and is known from IDPs (Dai and Bradley, 2001). If some individual fragments produced by disruption of an incident comet-dust particle contained primary metal, along-track variations in Fe/S (Fig. 10), (Fe + Ni)/S (Fig. 11), and possibly Fe/Mg (Fig. 9), may be due to association of Fe with (denser) metal and the greater penetration of denser, metal-rich grains. Finally, if Fe-sulfides are not thermally modified and depleted of S during disruption in the bulb but are melted and have some of their initial ferrous iron (hosted by cometary sulfides and/or silicates) reduced to metallic Fe (Leroux et al. 2008a, 2009; Rietmeijer et al. 2008) in transit through the stylus, grains in the stylus may be both depleted of S and density sorted.

In Track 35, Fe-monosulfides in bulbs were apparently melted but did not lose S, whereas Fe-monosulfides leaving the bulb and transiting the stylus were chemically modified by loss of volatile sulfur. Our results indicate S loss from melted grains in Track 35, but we cannot exclude the possibility that the evolved S may have been redistributed deep into surrounding aerogel rather than being actually lost from the aerogel (Flynn et al. 2006; Lanzirotti et al. 2008; Stephan 2008). Furthermore, sulfur behavior may vary not only along-track as reported here, but may also vary among different tracks. In a number of other Stardust aerogel tracks there is no along-track variation in S abundance (Flynn et al. 2006; Lanzirotti et al. 2008) like that observed here, but overall S abundances are low relative to CI and relative to mission data from comet 1P/Halley, suggesting S volatilization during aerogel capture (Flynn et al. 2006; Lanzirotti et al. 2008; Stephan 2008; Flynn 2008; Ishii et al. 2008b). The largest beads in grain C2004,1,44,1,3 have the lowest S abundances (Rietmeijer et al. 2008), suggesting either that sulfide minerals in the largest beads lost the most S during aerogel capture or that the largest beads had the lowest initial S abundances (and possibly consisted pre-capture of metal rather than sulfide) before melting. Leroux et al. (2000) report that the smallest (<20 nm diameter) beads in silicate-dominated shock melts with quenched metal-sulfide objects in a shocked ordinary chondrite are dominantly Fe sulfide, whereas larger (>20 nm diameter) beads contain appreciable Fe-Ni metal and are therefore have higher Fe:S ratios than the smaller beads. Comparable observations do not yet exist for other grains from any other Stardust aerogel tracks.

### *Differential Preservation of Pre-Capture Compositional Attributes Along-Track*

All five Stardust allocations examined for this study were melted grains (*sensu* Leroux et al. 2008a; amorphous grains of Zolensky et al. 2006); only grain 16 contained a very few angular metal-sulfide grains that may have not been completely melted during aerogel capture. In all other ways, melted grains from different parts of Track 35 are visually identical, indicating commonality of the basic melting-cooling processes during aerogel capture. However, melted grains from the bulb-stylus transition and the stylus differ compositionally from melted grains in the bulb in several important ways.

Increases in Fe relative to other elements with position in Track 35 (bulb versus bulb-stylus transition versus stylus, Fig. 7; and measured penetration depth, Figs. 9 and 10) are (as discussed above) consistent with density sorting of fragments produced during disruption of the fragile incident aggregate. Thus, different density fractions of preferentially melted material from the incident aggregate particle are non-uniformly distributed along track.

Melting and cooling appear to have had different effects on melted grains from different parts of Track 35. Melted grains in the bulb (grains 16 and 24; filled circles on Figs. 6 and 7) consistently have S abundances at or above those for stoichiometric FeS. This is consistent with any or all of the following:

1. The S in these melted grains is hosted in sulfides with Fe/S ratios less than one (e.g., Fe-deficient defect structures such as pyrrhotite, $Fe_{(1-x)}S$, or Fe-deficient solid-solution minerals such as pentlandite, (Fe,Ni)S). In this context, note that the average Fe/S ratio in melted grains (16 and 24) from the bulb is 0.89 (Fig. 10). As noted above, pyrrhotite occurs both as an unmodified comet mineral and as a product of aerogel-capture melting and quenching in Stardust allocations examined to date.
2. Some Fe in the melted grains from the bulb is hosted in non-sulfides (metal and/or silicate glass after silicate minerals). The x-intercept of approximately 0.1 Fe/Mg at zero S on Fig. 7 is consistent with approximately 10% total Fe being hosted in non-sulfides. As noted above, kamacite can occur both as an unmodified comet mineral and as a product of aerogel-capture melting and quenching in Stardust allocations examined to date. If all non-sulfide Fe in melted grains from the bulb was originally hosted in silicates, those silicates contained

approximately 90 at % Mg and 10 at % Fe; if some Fe was metal-hosted, associated silicates would be even poorer in Fe and richer in Mg. Either scenario for the host phases of the small amount of non-sulfide-hosted Fe (non-sulfide Fe in silicates only, or non-sulfide Fe in metal and Fe-poorer, Mg-richer silicate) is consistent with the dominance of Mg-rich olivine and pyroxene compositions in unmelted Stardust grains (Zolensky et al. 2006, 2008b).

Melted grains (open circles in Fig. 6, inverted triangles in Fig. 7) in the bulb-stylus transition (grains 51 and 52) and the stylus (grain 42) consistently have S abundances below those for stoichiometric FeS. This is consistent with S loss (relative to Fe and Mg) from these melted grains. The S/Mg ratio at zero Fe (Fig. 7) is consistent with the inferred association of Mg and S under extremely reducing conditions inferred by Leroux et al. (2009) from different allocations of the same two bulb-stylus transition grains (51 and 52) examined here. Melted grains from the bulb form a different population (e.g., Figs. 6 and 7) with different Fe-Mg-S relationships.

These results indicate some systematic along-track biases in otherwise identical melted (amorphous) grains. More dense (more Fe-rich) fragments penetrated further into the aerogel (Table 3; Figs. 7, 9), and experienced more S loss (Fig. 10), more reduction of Fe to metal (Leroux et al. 2009), and a stronger association of S with Mg (Fig. 7) indicative of extreme reducing conditions (Leroux et al. 2009) than the melted grains in the bulb. In contrast, less dense (more Mg-rich, Fe-poor) fragments, with most Fe associated with S in substoichiometric Fe-sulfides such as pyrrhotite and the remaining Fe in Mg-rich silicates and/or minor amounts of kamacite, were dispersed primarily along the walls of the bulb (Table 3; Figs. 7, 9). Thus, the melted grains with the least-modified compositional attributes are in the bulb, but preferentially represent only the most Mg-rich, Fe-poor portion of the density-sorted fragment population produced by grain disruption.

## SUMMARY AND CONCLUSIONS

All melted grains from Track 35 examined by transmission electron microscopy in this study resemble numerous other Stardust melted grains, consisting largely of a texturally and compositionally heterogeneous emulsion of metal/sulfide beads nanometers to tens of nanometers in diameter in a silica-rich vesicular glassy amorphous material (Zolensky et al. 2006; Brownlee et al. 2006; Ishii et al. 2008b; Leroux et al. 2008a; Tomeoka et al. 2008). The observed textures of individual phases and phase assemblages are consistent with silicate/metal-sulfide immiscibility and metal/sulfide immiscibility and rapid solidification of immiscible metal/sulfide droplets and the host silicate melt. The vast majority of the metal/sulfide beads are spherical. Textures of some non-spherical beads indicate that some large drops of molten metal-sulfide were in translational and rotational motion, and stretching and breaking, at the time they solidified. Textures of compound beads are more consistent with inertial fissioning of molten droplets than with coalescence. Textures of other non-spherical beads indicate they solidified from lenses of immiscible (metal-sulfide) liquid at the silicate-melt/vesicle (vapor) interface after cessation of relative motion between comet-dust fragments and the aerogel capture medium.

Compositions of sulfides and metal in individual droplets in (melted) grain 16 alone span much of the range of phases and compositions observed in the entire population of Stardust grains examined to date. Fe-monosulfides appear to be ubiquitous in melted grains from Track 35, as is the case for many previously studied Stardust melted grains. Textures in some bead cores suggest incomplete melting of the core mineral. Such minerals may be cometary minerals, rather than products of melting during aerogel capture. Grains 16 and 24 in Track 35 are unique among Stardust melted grains examined to date in the abundance of high-Ni, low-S metal/sulfide inclusions. Mineral associations reported in the literature suggest that pyrrhotite and kamacite each occur both in grains apparently unmodified by aerogel capture and in extensively melted grains, and may therefore have both cometary and capture-related origins. Taenite occurs in grains apparently unmodified by aerogel capture, and is not known from any other track including those with extensively melted grains, suggesting taenite is cometary in origin and does not form during aerogel capture.

The morphology of Track 35 suggests the incident comet dust particle was a fragile aggregate of easily fragmented material with some inclusions of mechanically stronger material. Chondrule-like objects with carbonaceous-chondrite affinities co-existed with fine-grained material of CI bulk composition (that preferentially melted and then quenched to form the melted glassy grains) in the incident comet-dust particle that formed Track 35.

Bulk compositions of five melted, glassy grains (two from the bulb, two from the bulb-stylus transition region, and one from the stylus near the terminal particle) are chondritic, but vary systematically along the track. Despite the clear influence of pre-melting attributes on the compositional and textural properties of melted grains, some along-track variation is superimposed on the variation caused by pre-melting heterogeneity. Iron abundances and Fe/Mg ratios increase systematically with deeper penetration into the aerogel, possibly as a consequence of disruption of variably dense comet dust and deeper penetration of denser fragments. Positive correlation between Ni and S suggests Ni is hosted in or closely associated with sulfides in Track 35, unlike the hosting of Ni by olivine suggested for other tracks by previous workers. Correlation of Fe and S, and near-stoichiometric Fe:S ratios in the two melted grains from the

bulb, are consistent with widespread reports of Fe-monosulfides as a dominant constituent of the melted grains. Fe/S ratios are near unity in melted grains from the bulb of Track 35; this is consistent with the dominance of Fe-monosulfide minerals reported from Stardust materials, and suggests that Fe-sulfides in the bulb were dispersed and melted but did not lose S during formation of the bulb. Increases in Fe/S in grains from the bulb-stylus transition and even greater increases in grains from the stylus indicate that in those parts of the aerogel-capture track, S initially present as iron monosulfide may have been partially volatilized and lost from the melted grains during capture-melting of comet dust. Systematic increases in Fe/S and (Fe+Ni)/S from the bulb through the bulb-stylus transition and along the stylus toward the terminal particle are consistent with previously suggested redistribution of S during aerogel capture. Despite their extensive melting, melted grains from the bulb regions of Stardust tracks may preserve indigenous compositional attributes of the incident cometary particles better than similar-looking melted grains from farther along track.

*Acknowledgments*—Keiko Nakamura-Messenger prepared the ultramicrotomed TEM allocations and provided helpful information about the preparation process. Xudong Fan of MSU's CAM assisted with TEM/EDS analyses. We are grateful to Stardust Curator Michael E. Zolensky for the allocations, and to Bernard P. Boudreau, Mike Zolensky, Frans Rietmeijer, Hugues Leroux, Nathan Sanders, and Duncan Sibley for helpful discussions and correspondence. Mike Zolensky and an anonymous reviewer made numerous critical and helpful comments which greatly assisted our revisions of the manuscript. TEM beam time was supported by the MSU CAM.

*Editorial Handling*—Dr. Scott Sandford

## REFERENCES

Adamson A. W. 1990. *Physical chemistry of surfaces*, 5th ed. New York: John Wiley & Sons. 800 p.

Akahoshi Y., Kaji M., and Hata Hi. 2003. Measurement of mass, spray angle, and velocity distribution of fragment cloud. *International Journal of Impact Engineering* 29:845–853.

Anderson W. W. and Ahrens T. J. 1994. Physics of interplanetary dust capture via impact into organic polymer foams. *Journal of Geophysical Research* 99:E2063–2071.

Bastien R., Messenger K., See T. H., Warren J. L., and Zolensky M. E. 2006. Stardust Sample Catalog. http://curator.jsc.nasa.gov/stardust/sample_catalog.

Bernhard R. P., Hörz F., See T. H., and Warren J. L. 2001. Soft capture of Earth-orbiting hypervelocity particles with aerogel. *International Journal of Impact Engineering* 26:39–51.

Bradley J. P. 1988. Analysis of chondritic interplanetary dust thin-sections. *Geochimica et Cosmochimica Acta* 52:889–900.

Brownlee D., Tsou P., Aléon J., Alexander C. M. O'D., Araki T., Bajt S., Baratta G. A., Bastien R., Bland P., Bleuet P., Borg J., Bradley J. P., Brearley A., Brenker F., Brennan S., Bridges J. C., Browning N. D., Brucato J. R., Bullock E., Burchell M. J., Busemann H., Butterworth A., Chaussidon M., Cheuvront A., Chi M., Cintala M. J., Clark B. C., Clemett S. J., Cody G., Colangeli L., Cooper G., Cordier P., Daghlian C., Dai Z., D'Hendecourt L., Djouadi Z., Dominguez G., Duxbury T., Dworkin J. P., Ebel D. S., Economou T. E., Fakra S., Fairey S. A. J., Fallon S., Ferinni G., Ferroir T., Fleckenstein H., Floss C., Flynn G., Franchi I. A., Fries M., Gainsforth Z., Gallien J.-P., Genge M., Gilles M. K., Gillet P., Gilmour J., Glavin D. P., Gounelle M., Grady M. M., Graham G. A., Grant P. G., Green S. F., Grossemy F., Grossman L., Grossman J. N., Guan Y., Hagiya K., Harvey R., Heck P., Herzog G. F., Hoppe P., Hörz F., Huth J., Hutcheon I. D., Ignatyev K., Ishii H., Ito M., Jacob D., Jacobsen C., Jacobson S., Jones S., Joswiak D., Jurewicz A., Kearsley A. T., Keller L. P., Khodja H., Kilcoyne A. L. D., Kissel J., Krot A., Langenhorst F., Lanzirotti A., Le L., Leshin L. A., Leitner J., Lemelle L., Leroux H., Liu M.-C., Luening K., Lyon I., MacPherson G., Marcus M. A., Marhas K., Marty B., Matrajt G., McKeegan K., Meibom A., Mennella V., Messenger K., Messenger S., Mikouchi T., Mostefai S., Nakamura T., Nakano T., Newville M., Nittler L. R., Ohnishi I., Ohsumi K., Okudaira K., Papanastassiou D. A., Palma R., Palumbo M. E., Pepin R. O., Perkins D., Perronnet M., Pianetta P., Rao W., Rietmeijer F. J. M., Robert F., Rost D., Rotundi A., Ryan R., Sandford S. A., Schwandt C. S., See T. H., Schlutter D., Sheffield-Parker J., Simionovici A., Simon S., Sitnitsky I., Snead C. J., Spencer M. K., Stademann F. J., Steele A., Stephan T., Stroud R., Susini J., Sutton S. R., Suzuki Y., Taheri M., Taylor S., Teslich N., Tomeoka K., Tomioka N., Toppani A., Trigo-Rodríguez J. M., Troadec D., Tsuchiyama A., Tuzzolino A. J., Tyliszczak T., Uesugi K., Velbel M., Vellenga J., Vicenzi E., Vincze L., Warren J., Weber I., Weisberg M., Westphal A. J., Wirick S., Wooden D., Wopenka B., Wozniakiewicz P., Wright I., Yabuta H., Yano H., Young E. D., Zare R. N., Zega T., Ziegler K., Zimmerman L., Zinner E., and Zolensky M. 2006. Comet 81P/Wild 2 under a microscope. *Science* 314:1711–1716.

Burchell M. J., Thomson R., and Yano H. 1999. Capture of hypervelocity particles in aerogel: in ground laboratory and low earth orbit. *Planetary and Space Science* 47:189–204.

Burchell M. J., Graham G., and Kearsley A. 2006. Cosmic dust collection in aerogel. *Annual Reviews of Earth and Planetary Sciences* 34:385–428.

Burchell M. J., Fairey S. A. J., Wozniakiewicz P., Brownlee D. E., Hörz F., Kearsley A. T., See T. H., Tsou P., Westphal A., Green S. F., Trigo-Rodríguez J. M., and Dominguez G. 2008. Characteristics of cometary dust tracks in Stardust aerogel and laboratory calibrations. *Meteoritics & Planetary Science* 43:23–40.

Burnett D. S. 2006. NASA returns rocks from a comet. *Science* 314: 1709–1710.

Curran D. R. 1997. Simple fragment size and shape distribution formulae for explosively fragmenting munitions. *International Journal of Impact Engineering* 20:197–208.

Dai Z. R. and Bradley J. P. 2001. Iron-nickel sulfides in anhydrous interplanetary dust particles. *Geochimica et Cosmochimica Acta* 65:3601–3612.

Davies J. T. and Rideal E. K. 1963. *Interfacial phenomena*. New York: Academic Press.

Dominguez G., Westphal A. J., Jones S. M., and Phillips M. L. F. 2004. Energy loss and impact cratering in aerogels: Theory and experiment. *Icarus* 172:613–624.

Fischer P. and Erni P. 2007. Emulsion drops in external flow fields – The role of liquid interface. *Current Opinion in Colloid & Interface Science* 12:196–205.

Flynn G. J. 2008. Physical, chemical, and mineralogical properties of

comet 81P/Wild 2 particles collected by Stardust. *Earth, Moon, and Planets* 102:447–459.

Flynn G. J., Bluet P., Borg J., Bradley J. P., Brenker F. E., Brennan S., Bridges J., Brownlee D. E., Bullock E. S., Burghammer M., Clark B. C., Dai Z. R., Daghlian C. P., Djouadi Z., Fakra S., Ferroir T., Floss C., Franchi I. A., Gainsforth Z., Gallien J.-P., Gillet P., Grant P. G., Graham G. A., Green S. F., Grossemy F., Heck P. R., Herzog G. F., Hoppe P., Hörz F., Huth J., Ignateyev K., Ishii H. A., Janssens K., Joswiak D., Kearsley A. T., Khodja H., Lanzirotti A., Leitner J, Lemelle L., Leroux H., Luening K., MacPherson G. J., Marhas K. K., Marcus M. A., Matrajt G., Nakamura T., Nakamura-Messenger K., Nakano T., Newville M., Papanastassiou D. A., Piantetta P., Rao W., Riekel C., Rietmeijer F. J. M., Rost D., Schwandt C. S., See T. H., Sheffield-Parker J., Simionovici A., Sitnitsky I., Snead C. J., Stadermann F. J., Stephan T., Stroud R. M., Susini J., Suzuki Y., Sutton S. R., Taylor S., Teslich N., Troadec D., Tsou P., Tsuchiyama A., Uesugi K., Vekemans B., Vicenzi E. P., Vincze L., Westphal A. J., Wozniakiewicz P., Zinner E., and Zolensky M. E. 2006. Elemental compositions of comet 81P/Wild 2 samples collected by Stardust. *Science* 314:1731–1734.

Hörz F., Zolensky M. E., Bernhard R. P., See T. H., and Warren J. L. 2000. Impact features and projectile residues in aerogel exposed on Mir. *Icarus* 147:559–579.

Hörz F., Bastien R., Borg J., Bradley J. P., Bridges J. C., Brownlee D., Burchell M. J., Chi M., Cintala M. J., Dai Z. R., Djouadi Z., Dominguez G., Economou T. E., Fairey S. A. J., Floss C., Franchi I. A., Graham G. A., Green S. F., Heck P., Hoppe P., Huth J., Ishii H., Kearsley A. T., Kissel J., Leitner J., Leroux H., Marhas K., Messenger K., Schwandt C. S., See T. H., Snead C. J., Stademann F. J., Stephan T., Stroud R., Teslich N., Trigo-Rodríguez J. M., Tuzzolino A. J., Troadec D., Tsou P., Warren J., Westphal A. J., Wozniakiewicz P., Wright I., and Zinner E. 2006. Impact features on Stardust: Implications for comet 81P/Wild 2 dust. *Science* 314:1716–1719.

Ishii H. A., Bradley J. P., Dai Z. R., Chi M., Kearsley A. T., Burchell M. J., Browning N. D., and Molster F. 2008a. Comparison of comet 81P/Wild 2 dust with interplanetary dust from comets. *Science* 319:447–450.

Ishii H. A., Brennan S., Bradley J. P., Luening K., Ignatyev K., and Pianetta P. 2008b. Recovering the elemental composition of comet Wild 2 dust in five Stardust impact tracks and terminal particles in aerogel. *Meteoritics & Planetary Science* 43:215–231.

Keller L. P., Bajt S., Baratta G. A., Borg J., Bradley J. P., Brownlee D. E., Busemann H., Brucato J. R., Burchell M., Colangeli L., D'Hendecourt L., Djouadi Z., Ferrini G., Flynn G., Franchi I. A., Fries M., Grady M. M., Graham G. A., Grossemy F., Kearsley A., Matrajt G., Nakamura-Messenger K., Mennella V., Nittler L., Palumbo M. E., Stadermann F. J., Tsou P., Rotundi A., Sandford S. A., Snead C., Steele A., Wooden D., and Zolensky M. 2006. Infrared spectroscopy of comet 81P/Wild 2 samples returned by Stardust. *Science* 314:1728–1731.

Lanzirotti A., Sutton S. R., Flynn G. J., Newville M., and Rao W. 2008. Chemical composition and heterogeneity of Wild 2 cometary particles determined by synchrotron X-ray fluorescence. *Meteoritics & Planetary Science* 43:187–213.

Leroux H., Doukhan J.-C., and Guyot F. 2000. Metal-silicate interaction in quenched shock-induced melt of the Tenham L6-chondrite. *Earth and Planetary Science Letters* 179:477–487.

Leroux H., Libourel G., Lemelle L., and Guyot F. 2003. Experimental study and TEM characterization of dusty olivines in chondrites: Evidence for formation by in situ reduction. *Meteoritics & Planetary Science* 38:81–94.

Leroux H., Rietmeijer F. J. M., Velbel M. A., Brearley A. J., Jacob D., Langenhorst F., Bridges J. C., Zega T. J., Stroud R. M., Cordier P., Harvey R. P., Lee M., Gounelle M., and Zolensky M. E. 2008a. A TEM study of thermally modified comet 81P/Wild 2 dust particles by interactions with the aerogel matrix during the Stardust capture process. *Meteoritics & Planetary Science* 43:97–120.

Leroux H., Jacob D., Stodolna J., Nakamura-Messenger K., and Zolensky M. E. 2008b. Igneous Ca-rich pyroxene in comet 81P/Wild 2. *American Mineralogist* 93:1933–1936.

Leroux H., Roskosz M., and Jacob D., 2009. Oxidation state of iron and extensive redistribution of sulfur in thermally modified Stardust particles. *Geochimica et Cosmochimica Acta* 73:767–777.

Matrajt G. and Brownlee D. E. 2006. Acrylic embedding of Stardust particles encased in aerogel. *Meteoritics & Planetary Science* 41: 1715–1720.

Mitchell T. J., Kendall M. A. F., and Bellhouse B. J. 2003. A ballistic study of micro-particle penetration to the oral mucosa. *International Journal of Impact Engineering* 28:581–599.

Nakamura T., Tsuchiyama A., Akaki T., Uesugi K., Nakano T., Takeuchi A., Suzuki Y., and Noguchi T. 2008a. Bulk mineralogy and three-dimensional structures of individual Stardust particles deduced from synchrotron X-ray diffraction and microtomography analysis. *Meteoritics & Planetary Science* 43: 247–259.

Nakamura T., Noguchi T., Tsuchiyama A., Ushikubo T., Kita N. T., Valley J. W., Zolensky M. E., Kakazu Y., Sakamoto K., Mashio E., Uesugi K., and Nakano T. 2008b. Chondrule-like objects in short-period comet 81P/Wild 2. *Science* 321:1664–1667.

Rietmeijer F. J. M. 2008. Natural variation in comet-aggregate meteoroid compositions. *Earth, Moon, and Planets* 102:461–471.

Rietmeijer F. J. M., Nakamura T., Tsuchiyama A., Uesugi K., Nakano T., and Leroux H. 2008. Origin and formation of iron silicide phases in the aerogel of the Stardust mission. *Meteoritics & Planetary Science* 43:121–134.

Roskosz M., Leroux H., and Watson H. C., 2009. Thermal history, partial preservation and sampling bias recorded by Stardust cometary grains during their capture. *Earth and Planetary Science Letters* 273:195–202.

Stephan T. 2008. Assessing the elemental composition of comet 81P/Wild 2 by analyzing dust collected by Stardust. *Space Science Reviews* 138:247–258.

Stephan T., Flynn G. J., Sandford S. A., and Zolensky M. E. 2008. TOF-SIMS analysis of cometary particles extracted from Stardust aerogel. *Meteoritics & Planetary Science* 43:285–298.

Stone H. A. 1994. Dynamics of drop deformation and breakup in viscous fluids. *Annual Review of Fluid Mechanics* 26:65–102.

Summerlin L. B. 1977. *Skylab, classroom in space*. NASA Special Publication SP-401. 182 p.

Tomeoka K., Tomioka N., and Ohnishi I. 2008. Silicate minerals and SiO glass in comet Wild 2 samples: Transmission electron microscopy. *Meteoritics & Planetary Science* 43:273–284.

Trigo-Rodríguez J. M., Dominguez G., Burchell M. J., Hörz F., and Llorca J. 2008. Bulbous tracks arising from hypervelocity capture in aerogel. *Meteoritics & Planetary Science* 43:75–86.

Trucano T. G. and Grady D. E. 1995. Impact shock and penetration fragmentation in porous media. *International Journal of Impact Engineering* 17:861–872.

Velbel M. A. 2004. Laboratory and homework exercises in the geochemical kinetics of mineral-water reaction: Rate law, Arrhenius activation energy, and the rate-determining step in the dissolution of halite. *Journal of Geoscience Education* 52:52–59.

Zolensky M. E. and Thomas K. L. 1995. Iron- and iron-nickel sulfides in chondritic interplanetary dust particles. *Geochimica et Cosmochimica Acta* 59:4707–4712.

Zolensky M. E., Zega T. J., Yano H., Wirick S., Westphal A. J., Weisberg M. K., Weber I., Warren J. L., Velbel M. A., Tsuchiyama A., Tsou P., Toppani A., Tomioka N., Tomeoka K.,

Teslich N., Taheri M., Susini J., Stroud R., Stephan T., Stadermann F. J., Snead C. J., Simon S. B., Simionovici A., See T. H., Robert F., Rietmeijer F. J. M., Rao W., Perronnet M. C., Papanastassiou D. A., Okudaira K., Ohsumi K., Ohnishi I., Nakamura-Messenger K., Nakamura T., Mostefaui S., Mikouchi T., Meibom A., Matrajt G., Marcus M. A., Leroux H., Lemelle L., Le L., Lanzirotti A., Langenhorst F., Krot A., Keller L. P., Kearsley A., Joswiak D., Jacob D., Ishii H., Harvey R., Hagiya K., Grossman L., Grossman J. N., Graham G. A., Gounelle M., Gillet P., Genge M. J., Flynn G. J., Ferroir T., Fallon S., Ebel D. S., Dai Z. R., Cordier P., Chi M., Butterworth A. L., Brownlee D. E., Browning N., Bridges J. C., Brennan S., Brearley A., Bradley J. P., Bland P., and Bastien R. 2006. Mineralogy and petrology of comet 81P/Wild 2 nucleus samples. *Science* 314:1735–1739.

Zolensky M., Nakamura-Messenger K., Fletcher L., and See T. 2008a. Curation, spacecraft recovery, and preliminary examination for the Stardust mission: A perspective from the curatorial facility. *Meteoritics & Planetary Science* 43:5–21.

Zolensky M., Nakamura-Messenger K., Rietmeijer F., Leroux H., Mikouchi T., Ohsumi K., Simon S., Grossman L., Stephan T., Weisberg M., Velbel M., Zega T., Stroud R., Tomeoka K., Ohnishi I., Tomioka N., Nakamura T., Matrajt G., Joswiak D., Brownlee D., Langenhorst F., Krot A., Kearsley A., Ishii H., Graham G., Dai Z. R., Chi M., Bradley J., Hagiya K., Gounelle M., and Bridges J. 2008b. Comparison of Wild 2 particles to chondrites and IDPs. *Meteoritics & Planetary Science* 43:261–272.